NOVA SCHOOL OF SCIENCE & TECHNOLOGY

DEPARTMENT OF PHYSICS

SOFIA HASSANE RIBEIRO

Bachelor of Science in Biomedical Engineering

INCORPORATION OF 4-AMINOPIRIDINE IN MEMBRANES FOR SKIN REINNERVATION

Dissertation

MASTER IN BIOMEDICAL ENGINEERING

NOVA University Lisbon

September, 2024

NOVA SCHOOL OF SCIENCE & TECHNOLOGY

DEPARTMENT OF PHYSICS

INCORPORATION OF 4-AMINOPIRIDINE IN MEMBRANES FOR SKIN REINNERVATION

SOFIA HASSANE RIBEIRO

Bachelor of Science in Biomedical Engineering

Adviser: Tânia Vieira
Researcher, NOVA University Lisbon

Co-advisers: Célia Henriques
Associate Professor, NOVA University Lisbon

Examination Committee:

Chair: Susana Sério,
Assistant Professor, NOVA University Lisbon

Rapporteurs: Paula Soares,
Principal Investigator, NOVA University Lisbon

Adviser: Tânia Vieira,
Researcher, NOVA University Lisbon

Dissertation
MASTER IN BIOMEDICAL ENGINEERING

NOVA University Lisbon
September 2024

INCORPORATION OF 4-AMINOPIRIDINE IN MEMBRANES FOR SKIN REINNERVATION

À minha Mãe, que sempre me apoiou em tudo.

ACKNOWLEDGMENTS

I would like to express my deepest gratitude to my advisor, Doctor Tânia Vieira, for her unwavering support, remarkable patience, and constant guidance throughout this journey. It has been an immensely valuable experience to have had the opportunity to work under your supervision, you have been the most exceptional mentor. I will always look up to you for your professionalism, your expertise, wisdom, and dedication.

I am also thankful to my co-supervisor, Professor Doctor Célia Henriques, for her generous support, your knowledge and encouragement have greatly contributed to the development and successful completion of this project.

Additionally, I would like to thank to Professor Doctor Jorge Carvalho Silva for his feedback during monthly meetings and for welcoming me into the laboratory.

I would also like to acknowledge, with heartfelt gratitude, everyone at the GREAT lab, for the warm and welcoming environment you fostered. A special appreciation goes to Vilão, Catarina Sénior, Catarina Júnior, and Sofia.

To my dearest friends, Lucas, Dourado, and Jorge, thank you for making this journey so much more enjoyable, for the wonderful moments and spontaneous hangouts.

To my love, André, thank you for standing by my side through it all. You were my strength when I needed it most, constantly encouraging me. Thank you for being my home.

To my brother for bringing Baushi along and for always being my source of laughter.

Finally, but definitely not least, my gratitude goes to my loving parents.

Thank you, Dad, for always being there for me, your belief in me have made all possible. Thank you for the moments we spent together walking shelter dogs during my breaks at work.

Thank you, Mom, for always being there for me. I wouldn't be where I am today without your constant encouragement, guidance, support, love, and belief in me. I am forever grateful.

You've been my strength and my inspiration to keep pushing forward. I will always look up to you as my role model, my greatest source of wisdom.

ABSTRACT

Significant advances have been made in investigations regarding solutions for skin regeneration, however, challenges persist, particularly in restoring sensitivity and function to severely damaged skin. 4-aminopyridine (4-AP) has been identified as a drug that promotes reinnervation, making it a promising candidate for dermal regeneration and reinnervation. In this study, 4-AP was incorporated for the first time into electrospun polymeric membranes of chitosan (CS), poly(ε-caprolactone) (PCL) and CS/PCL. This approach aims to contribute to the development of an innovative skin treatment, offering a potential alternative to conventional drug delivery methods. The incorporation of 4-AP resulted in an increase in porosity for the PCL and CS membranes, swelling ratio, and a reduction in fiber diameter to a level that could have a positive impact on wound healing. The PCL and CS/PCL membranes followed release kinetics consistent with the Higuchi model. Concentrations of 4-AP below 0.5 mM demonstrated no cytotoxicity in HFFF2, HaCaT, and SH-SY5Y cells, which were used as cell line models for fibroblasts, keratinocytes and neural cells, respectively. CS/PCL membranes supported the highest cell proliferation, as confirmed by adhesion/proliferation assays and fluorescence microscopy images. 4-AP slowed the wound closure process in HaCaT and HFFF2 cells. Differentiation was observed in PCL/4-AP membranes with retinoic acid (RA), suggesting that 4-AP may enhance the effects of RA. However, additional replicates are needed to confirm that 4-AP induces SH-SY5Y cell differentiation on the membranes.

Keywords: Skin regeneration, 4-aminopyridine, Wound healing assay, Electrospinning, Membranes, Drug release, Cellular differentiation

RESUMO

Na investigação de soluções que promovem a regeneração da pele, têm sido desenvolvidos avanços notáveis, contudo continuam a existir desafios, sobretudo na restauração da sensibilidade e função de pele gravemente danificada. A 4-aminopiridina (4-AP) foi identificada como um fármaco que promove a reinervação, sendo promissor para a regeneração e reinervação dérmica. Neste estudo, a 4-AP foi incorporada pela primeira vez em membranas poliméricas eletrofiadas de quitosano (CS), poli(ε-caprolactona) (PCL) e CS/PCL, pretendendo contribuir para o desenvolvimento de um tratamento inovador para a pele, oferecendo uma alternativa aos métodos convencionais de administração de fármacos. A incorporação de 4-AP resultou num aumento da porosidade das membranas de PCL e CS, da taxa de absorção de fluidos e numa redução do diâmetro das fibras para um nível que pode ter um impacto positivo na cicatrização de feridas. As membranas de PCL e CS/PCL seguem uma cinética de libertação de acordo com o modelo de Higuchi. Concentrações inferiores a 0,5 mM de 4-AP não demonstraram citotoxicidade nas células HFFF2, HaCaT e SH-SY5Y, utilizadas como modelos de linhas celulares para fibroblastos, queratinócitos e células neurais, respetivamente. Membranas de CS/PCL suportaram a maior proliferação celular, conforme testes de adesão/proliferação e imagens de microscopia de fluorescência. A 4-AP abrandou o processo de fechar a ferida simulada nas células HaCaT e HFFF2. Foi observada diferenciação nas membranas de PCL/4-AP com ácido retinoico (RA), sugerindo que a 4-AP pode potenciar os efeitos do RA. No entanto, são necessários ensaios adicionais para avaliar se a 4-AP induz diferenciação das células SH-SY5Y nas membranas.

Palavras chave: Regeneração da pele, 4-aminopiridina, Ensaios de cicatrização de feridas, Eletrofiação, Membranas, Libertação de fármacos

CONTENTS

LIST OF FIGURES

List of Tables

ABBREVIATIONS

3D	Three-dimensional
4-AP	4-aminopyridine
BSA	Bovine serum albumin
CNS	Central nervous systems
CS	Chitosan
DAPI	4',6-diamidino-2-phenylindole
ECM	Extracellular matrix
F-actin	Filamentous actin
FBS	Fetal bovine serum
FDA	US Food and Drug Administration
HaCaT	Keratinocytes cells
HFFF2	Fibroblasts cells
IUPAC	International Union of Pure and Applied Chemistry
MAP-2	Microtubule associated protein-2
MS	Multiple sclerosis
n	number of samples
PBS	Phosphate-buffered saline
PCL	Poly-ε-caprolactone

PGA	Polyglycolic acid
PLLA	Poly(L-lactic acid)
PNI	Peripheral nerve injury
PNS	Peripheral nervous systems
TE	Tissue engineering
SCI	Spinal cord injury
SCs	Schwann cells
SEM	Scanning electron microscopy
SH-SY5Y	Neuroblastoma cells
SS	Skin substitutes
UV-VIS	Ultraviolet–visible spectroscopy

1

INTRODUCTION

1.1 Context and Motivation

The skin serves as an essential defence against contaminants and microorganisms in the environment, safeguards against dehydration and has a fundamental role in sensory detection. Loss of skin integrity due to injuries or illnesses can lead to substantial physiological disruption and significant disability or even death. Skin substitutes (SS) are emerging replacements for conventional injury healing and cutaneous regeneration strategies. Various SS with distinct characteristics have been developed [2] to provide barrier function, improved protection against microorganisms, pain relief, and promote proper healing [3]. However, commercially available SS face challenges including low mechanical integrity, immunological rejection, inadequate vascularization, scarring [3], and lack of reinnervation [4], [5], [6]. The goal is to regenerate tissues, restoring both functional and structural characteristics to pre-injury levels.

The skin and its appendages are innervated by the peripheral nervous system (PNS) [7], as shown in Figure 1.

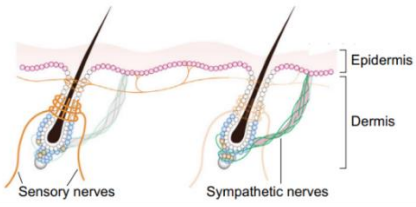

Figure 1- The skin and its appendages are innervated by nerves from the PNS [7].

Currently, peripheral nerve repair primarily relies on surgical intervention combining microsuture repair and the usage of nerve grafts (in the case of wider nerve gaps). The clinical use of autologous nerve grafts is more suitable, when this is not feasible, allogenic nerve grafts of cadaveric origin are primarily utilized [8]. However, allogenic grafts have disadvantages like

length mismatch, neuroma formation, limited donor nerve availability [9], and donor site morbidity [8]. An additional therapeutic method to enhance reinnervation during the healing process is using biomaterials as artificial nerve conduits to guide nerve growth and prevent complications at the injury site [10], [11], [12]. Current nerve conduits, whether produced from natural or synthetic biomaterials, do not lead to complete functional recovery [13]. An alternative treatment approach involves cell or exosome therapy, which can be implemented without biomaterial support or, in the tissue engineering (TE) domain, with its incorporation into a biomaterial as a scaffold. Recently, these structures, which can be produced as matrices of nanofibers, have been the subject of investigation and developed to offer a solution with diverse functionalities, such as targeted drug delivery and controlled drug release. Successful TE strategies involve the appropriate combination of cells and scaffolds, as well as drugs and other factors, to replicate tissue function or stimulate regeneration [14] and innervation effectively.

This in vitro study aims to develop membranes with a morphology like the extracellular matrix, enabling the controlled local delivery of 4-AP. As such, it offers an alternative to traditional drug administration for skin regeneration and reinnervation.

1.2 Skin structure, regeneration and reinnervation

Skin exhibits a complex structure with distinct layers. The avascular epidermis, composed of Langerhans cells, keratinocytes that produce keratin, and melanocytes, forms the outer layer of the skin. Beneath it, the dermis, rich in blood vessels and specialized glands, is maintained by fibroblasts. These fibroblasts are responsible for synthesizing type I collagen, contributing to the extracellular matrix (ECM) [2], [5] , and play a crucial role in depositing other essential components like elastin and proteoglycans [5]. The hypodermis, integrated into the endocrine system, predominantly consists of adipose cells, acting as a lipid barrier and playing an important part in processes such as reepithelization, wound healing, and angiogenesis [5]. The stratified organization is vital for skin functionality like vascular growth and innervation [5].

Following skin injury, tissue restoration involves three phases: inflammation, proliferation, and remodelling [15], as depicted in Figure 2. Blood clotting forms a temporary shield against fluid loss and pathogens [15]. In the inflammatory phase, immunocompetent cells remove dead tissue. In the proliferation phase, growth factors secreted by inflammatory cells promote the proliferation of vascular endothelial cells and fibroblasts [15]. The fibrin matrix transitions to collagen, secreted by fibroblasts, with differentiation into myofibroblasts contributing to wound contraction [3]. Fibroblasts are essential for wound healing, contribute to

fibrosis, are involved in inflammatory processes, generate ECM, and influence the functions of immune cells [2]. The stage of blood vessel formation involves the migration of keratinocytes from the edges of the wound to the surface of the tissue, below the blood clot. The remodelling phase concludes with re-epithelialization and restoration of dermal tensile strength [3].

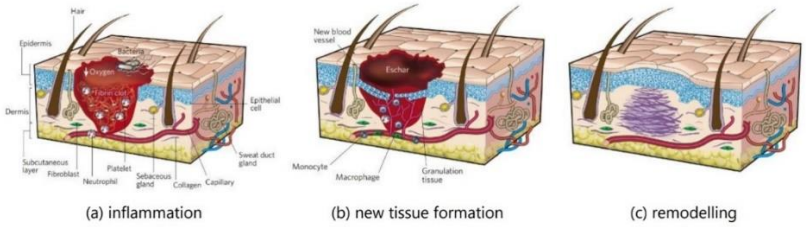

Figure 2- Common stages of wound repair [15].

The skin, a vastly responsive organ, is richly innervated throughout both the dermis and epidermis, as illustrated in Figure 1, allowing for the discrimination of pain, itching, thermal, and tactile sensations [4]. In the PNS and central nervous systems (CNS), myelin plays a crucial role in insulating axons to facilitate the rapid conduction of electrical impulses [16]. Glial support cells include Schwann cells (SCs) in the PNS [12], [17] and oligodendrocytes in the CNS [12]. The nervous system present in the skin primarily corresponds to sensory nerve endings. Cutaneous sensory nerve fibers transmit signals from sensory receptors to the integration center in the brain via the spinal cord, influencing various physiological and pathological functions of the skin [4]. Skin injury can result in peripheral nerve injury (PNI) and can lead to complications [12], [16], with palliative and rehabilitative care as the feasible choice [16].

1.3 Scaffolds for skin reinnervation

Scaffolds, as platforms for cell development, must fulfil essential functions by providing support for cells, facilitating oxygen exchange, and serving as delivery systems of nutrients, cytokines, growth factors and drugs for cells [18]. Therefore, it is important to develop and design synthetic ECM analogues with uniform 3D porous structure, designed with materials capable of replicating the physical, chemical, and physiological microenvironments of skin tissues. Thus, in TE, biomaterials play a key role, requiring biocompatibility, interconnected pores, and appropriate mechanical properties for effective wound healing and skin reinnervation. Synthetic biomaterials used for skin-replacement therapies, degradation process must not inhibit the acceptable progress of tissue regeneration and vascularization [6].

Considering that electrical stimulation promotes axon and neurite extension, as well as nerve regeneration, Baniasadi *et al.* [19] incorporated conductive polyaniline/graphene

nanoparticles into a chitosan (CS)/gelatin matrix, resulting in a porous scaffold with suitable conductivity, mechanical stability, and biocompatibility for neural repair. Another study with a CS/gelatin scaffold doped with phlorotannin [20] showed potential for tissue regeneration. The ability to influence cells through physical and chemical stimuli offers advantages towards regeneration [19]. The challenge lies in creating scaffolds that support regeneration while also modulating inflammation and promoting reinnervation. Electrical stimulation [21], is advantageous in PNI models. Therefore, it is expected that pharmacological drugs that may influence nerve conduction may contribute to nerve regeneration [21]. In the context of skin reinnervation, 4-aminopyridine (4-AP), an organic potassium channel blocker [22] emerges as promising drug to obtain this electrical stimulation.

1.3.1 Membranes as drug delivery systems

Multifunctional drug delivery systems have recently undergone significant development to integrate targeted delivery and controlled release. Polymeric nanoscale fibers have emerged as versatile carriers for drug incorporation. The main goal of drug therapy is to maintain optimal therapeutic concentrations at the target site. Polymeric membranes may enable prolonged drug release, enhancing therapeutic efficacy [23], [24]. The design of these systems requires a solid understanding of the drug release profile to ensure stability, consistency, and quality control. Factors such as composition of the vehicles, component interactions, and preparation methods influence drug release. Additionally, varying structure, charge, functional groups, or pH enhances stability, pharmacokinetics, and therapeutic efficacy. It is also imperative to explore both drug incorporation and the binding process to preserve the properties of the drug and the materials [25], [26], [27]. The drug release mechanism involves the release of surface-adsorbed drug, diffusion through the swollen polymer matrix, and polymer erosion, such as bond cleavage or hydrolysis, allowing prolonged release. Often, a combination of these processes governs the overall release profile [28]. Mathematical models simplify the calculation of quantitative data related to drug release, enabling the optimization of delivery system design and analysis. These models improve the understanding and prediction of drug release kinetics from polymeric structures, providing results that approximate real systems scenarios. The mathematical equations used in these models describe various processes, including diffusion and degradation, where solid matter dissolves in a solvent during drug release [29]. Representing the percentage of drug released at a given time t by Q, while Q_0 denotes the percentage of drug yet to be released, the zero-order rate equation, ($Q = k_0 t$), applies to drug delivery

systems with a constant release rate, k_0, unaffected by the concentration of the drug, ensuring consistent release over time. In contrast, the first-order equation ($ln(100 - Q) = ln(Q_0) - k_1t$) describes systems where the release rate, controlled by the constant k_1, declines as the drug concentration decreases. Higuchi's model [30] characterizes drug release from an insoluble matrix as a process driven by diffusion and is expressed by the equation ($Q = k_H t^{1/2}$), where k_H is a model parameter. The Peppas equation ($Log (Q/100) = k_p t^n$) addresses systems with non-linear release behaviours, with Q depending on the parameter k_p, a constant that accounts for the geometric and structural properties of the release system, and on the release exponent, n, which provides insight into the drug release mechanism [29]. Hixson–Crowell equation [31], ($Q_0^{1/3} - Q^{1/3} = K_{HC}t$), details release systems characterized by variations in diameter and surface area of particles [29].

1.3.2 Materials used for membranes production in TE

Natural polymers

In the realm of natural polymers, hyaluronic acid [14], collagen [5], [13], [32], gelatin [5], [20], [33], keratin [5], fibronectin [32], [34], and chitosan (CS) [13], [35] have been used in various TE applications. These biomaterials, exhibit high biocompatibility and demonstrate promising outcomes in skin wound healing, each with distinct characteristics and potential applications. Closely resembling materials of the human ECM, the favourable interaction with human tissues, underscores their potential therapeutic efficacy. However, they also present distinct limitations. For example, hyaluronan, while aiding in scar reduction [36] and improving conduction speed, axon count, and myelination when used in injectable polyethylene nerve guides implanted in the sciatic nerve of rats [37], has disadvantages such as excessive softness, substantial swelling [37], and poor cell binding properties [12]. Collagen is a predominant component of the ECM [38] but presents some drawbacks, such as rapid contraction[39] and degradation [40]. The high aqueous solubility of many natural polymeric scaffolds decreases the bioactive potential of these materials. Therefore, the implementation of cross-linking methods, encompassing physical and chemical approaches, is essential to reduce solubility and stabilize scaffolds [41].

Synthetic polymers

Various synthetic polymers, such as silicone, polyglycolic acid (PGA) [11], [13], poly(L-lactic acid) (PLLA) [5], [37], [42], [43] and poly-ε-caprolactone (PCL) [5], [41], have been used to promote PNS repair. All of them are biodegradable [42] and present excellent resistance to deformation and high flexibility [42], [44], making them suitable for scaffold fabrication.

However, limitations arise, for example in the case of PLLA it includes potential adverse effects of degradation products, such as lactic acid, on axonal growth and nerve function [37].

Composite biomaterials

Synthetic biomaterials are used in the manufacture of scaffolds due to their mechanical integrity [4] but have poor interaction with cells due to the absence of biological recognition sites [42]. They lack the inherent bioactivity that is uniquely provided by natural polymers [41], since their hydrophobic surfaces make them unsuitable for optimal cell adhesion and proliferation [45]. On the other hand, various natural materials, while biocompatible and biodegradable, often lack sufficient mechanical resistance. Considering these aspects, researchers explore composite materials to leverage the desirable properties of synthetic and natural materials [4], [45]. Consequently, scaffold modification with bioactive molecules, such as components of ECM (collagen, laminin, fibronectin) [32], [35] aims to establish a conducive biochemical environment for increased adhesion, proliferation, and differentiation of neuronal cells. Kijenska *et al.* [45] fabricated a composite scaffold involving poly (L-lactic acid)-co-poly(e-caprolactone/collagen(I/III) that exhibited mechanical properties and fiber orientation suitable for peripheral nerve regeneration and showed enhanced nerve stem cell proliferation *in vitro*. Gu *et al.* developed CS-PGA conduits, in a clinical case study, and achieved nerve regeneration, demonstrating that these materials are promising for neural repair [11].

1.3.2.1 Chitosan

Chitosan (CS), Figure 3, is a natural polysaccharide that is predominantly amorphous and nearly insoluble in water on account of its strong intermolecular hydrogen bonds between polymer chains [46]. However, it becomes soluble in aqueous solutions with a pH below 6, as the amino groups are protonated. Its solubility in alkaline solutions can be enhanced by chemical modifications, such as attaching carboxymethyl groups while maintaining its cationic nature [46].

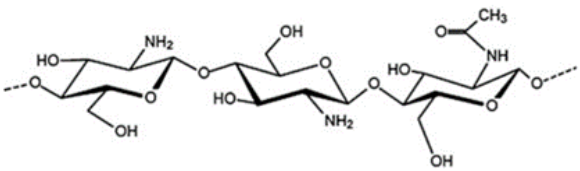

Figure 3- Chitosan chemical structure (with inactive units and acetylated units). Adapted from [47].

CS is biocompatible, non-toxic [48], bioadhesive [49], approved by the US Food and Drug Administration (FDA), making it an ideal biomaterial for healthcare applications, TE, and drug delivery systems. Its molecular structure includes functional groups like primary and secondary alcohols and amine (-NH_2) groups, which inhibit bacterial and fungal growth contributing to

CS's antimicrobial properties. CS's versatility extends to its ability to bind negatively charged bioactive molecules, influence blood coagulation, and accelerate wound healing [50]. With a structure similar to collagen, it has potential to enhance nerve regeneration [13] and is also hemostatic [20]. CS is biodegradable as it is metabolized by human enzymes like lysozyme [50]. Its structural similarity to glycosaminoglycans, along with its hydrophilic nature [50], makes CS an appealing material for TE scaffolds. Having been observed to contribute to re-epithelialization, it is used as the basis for a skin substitute [20]. In addition, CS has a significant applicability in drug delivery systems for the controlled release of therapeutics while ensuring compatibility with biological environments [46].

Modifications of CS, including cross-linking, and complexation [50], enhance its functionality for controlled drug delivery. Drug release from CS membranes is influenced by factors like polymer swelling, drug diffusion, and polymer erosion or degradation [46]. Drug encapsulation within CS membranes typically occurs through hydrogen bonds, Van der Waals forces and electrostatic interactions. These modifications alter the properties of CS membranes, significantly affecting their drug release profiles and enabling specialized therapeutics.

1.3.2.2 Poly-ε-caprolactone (PCL)

PCL, Figure 4, is a widely researched biocompatible synthetic polymer, with FDA approval for applications ranging from sutures to tissue regeneration. The rough surface properties of PCL [51] can be modified, making it ideal for optimizing tissue interface characteristics. These features enhance the interaction between the biomaterial and surrounding tissues, improving its effectiveness in TE applications [51]. Mechanical properties revealed flexibility and adaptability, making it suitable as a skin implant [52]. It is frequently used in electrospun scaffolds for biomedical purposes, with proven potential as a drug delivery system.

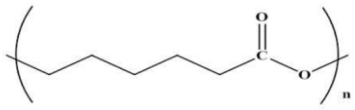

Figure 4- PCL chemical structure [53].

As a non-toxic aliphatic polyester, PCL provides structural stability [54] due to its ester linkages per monomer, leading to a longer degradation time *in vivo* when used as a biomaterial. Typically, PCL degrades over a period of two to three years in biological environments containing interstitial fluid. The enzyme lipase, present in interstitial fluid, aids in its enzymatic degradation by breaking down the ester linkages [53]. PCL degradation products are safely processed by the body's normal metabolic pathways [44], since these products such as lactic acid are converted into water and carbon dioxide [53].

1.3.2.3 Chitosan and Poly-ε-caprolactone

The combination of CS and PCL in electrospun scaffolds consists in a valuable material for TE applications [55]. *In vitro* and *in vivo* studies confirm that CS/PCL electrospun mats enhance wound healing more effectively than scaffolds made from either component alone [56]. Pal *et al* [57] combined CS/PCL nanofibrous layers impregnated with collagen to mimic dermal characteristics, as a skin substitute. In implantation *in vivo* and co-culture with fibroblast cells and keratinocytes *in vitro*, this structure showed efficacy in promoting re-epithelialization and the development of mature dermal tissue [57].These polymers with distinct chemical structures can interact through various types of chemical bonds, including hydrogen bonds between the CS amine (-NH_2) and hydroxyl (-OH) groups and the PCL carbonyl (C=O) groups, as well as dipole-dipole and Van der Waals interactions. These interactions, particularly hydrogen bonding, are essential for the formation of stable CS/PCL composites, affecting properties such as biocompatibility, biodegradability, and mechanical strength.

1.4 4-aminopyridine

4-aminopyridine (4-AP), IUPAC name: pyridine-4-amine, Figure 5, improves nerve impulse conduction in demyelinated lesions [58]. 4-AP with a molecular weight of 94.12 g/mol, contains a pyridine ring substituted by an amino group at position 4. Its pKa is 9.1 and in aqueous solutions at pH 11.4 it exists primarily as a protonated base. At physiological pH, around 98% of the molecules are protonated, forming a monocation. The delocalization of the ionic charge between each nitrogen prevents further protonation, making 4-AP a basic compound that is water-soluble and highly ionized under physiological conditions.

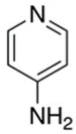

Figure 5- 4-aminopyridine [59].

Metabolically, 4-AP undergoes minimal transformation via hepatic enzymes, starting with hydroxylation to 3-hydroxy-4-AP. The majority of 4-AP is eliminated through renal excretion, with 90% excreted unchanged within 24h [60]. Pharmacologically, 4-AP blocks potassium channels [60] and modulates neuronal excitability in a dose-dependent way [61]. In terms of administration, 4-AP is currently approved by the FDA [62] under the brand name Fampyra® for managing symptoms of spinal cord injury (SCI) and demyelinating disorders like multiple sclerosis (MS) improving the patient's walking ability. The daily oral dose of 4-AP for human

treatment ranges between 10 and 30 mg [63]. Initially, 4-AP was delivered intravenously or through oral gelatin capsules in immediate-release forms, leading to rapid peak plasma concentrations and short duration in the system. Its toxicity is tied to these peak levels rather than total exposure [61]. Recently, a prolonged-release formulation like Fampyra® was developed to extend therapeutic effects, maintain lower peak plasma, reduce dosing frequency, and minimize adverse effects [61]. To optimize prolonged drug delivery, the employment of nanomembranes incorporating 4-AP could offer a more effective alternative to traditional drug applications. There are published studies where 4-AP has been incorporated into polymers. For example, Tseng *et al.* [21], demonstrated that 4-AP encapsulated in poly(lactic-co-glycolic acid) accelerated recovery and enhanced remyelination in rats. 4-AP promotes SCs and axon growth, *in vivo*, contributing to nerve regeneration and wound healing [21], [62]. In another research, Fallah-Darrehchi *et al.* [58] developed an electrospun poly (L-lactide-co-D, L-lactide), conduit containing 4-AP, suggesting its potential for nerve regeneration and demonstrating controlled 4-AP release.

1.5 Electrospinning

Among the various techniques used in manufacturing scaffolds, electrospinning, Figure 6, appears to be the most suitable method for fabricating fibers resembling the ECM of the skin. It provides control over the properties of the engineered scaffold like fiber diameter and orientation, which influence cell adhesion and proliferation, and nutrient transport [45]. Fibers with diameters ranging from micrometers to nanometers can be obtained [64]. The obtained membranes exhibit high porosity (60–90%) and interconnectivity among pores, which allow efficient supply of oxygen and nutrient to cells, while controlling exudate maintenance at the wound. The possibility of use various polymers offer versatility to the electrospun fibers [20]. Through several parameters adjustment, electrospinning enables the creation of scaffolds with a topography of aligned nanofibers and composite scaffolds suitable for nerve TE [45]. Electrospinning relies on polymer properties such as solubility and molecular weight [65].

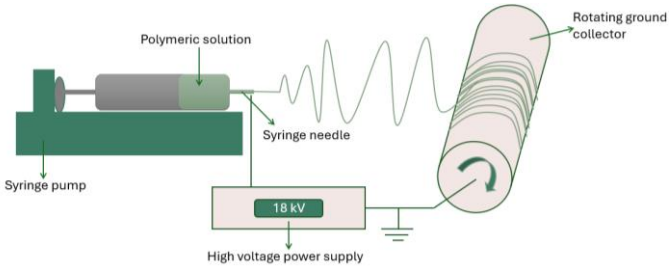

Figure 6- Scheme depicting an electrospinning experimental setup and process.

2

MATERIALS AND METHODS

All weighing was conducted using a Radwag XA 82/220 analytical balance (±0.1 mg uncertainty), except for solvent measurements, which were performed on a Radwag WPS 510/C/2 balance (±1 mg uncertainty). Image analysis was conducted using ImageJ.

2.1 Nanofibrous Membrane Production

2.1.1 Polymeric Solutions

Polymers selected for membrane production were CS (Chitopharm S, from Cognis, Mw = 500 kDa, degree of deacetylation = 75.5 %), and PCL (Sigma-Aldrich, Mn= 80000 Da). The following concentrations are expressed in percentage of polymer mass relative to total solution mass. All polymeric solutions weighted 10 g. A 10 wt% PCL solution was prepared in chloroform (Carlo Erba Reagents), with chloroform loss accounted by weighing after solution preparation and before fiber production. The CS solution consisted in 1.8 wt% CS and 0.4 wt % Poly(ethylene oxide) (PEO, Mw= 8 MDa, Sigma-Aldrich), dissolved in a 90:10 acetic acid (Fisher Scientific): water mixture. A combined CS and PCL solution contained 2 wt % CS, 2 wt % PCL and 0.25 wt % PEO, dissolved in a 90:10 acetic acid: water mixture [66]. All solutions were stirred using a magnetic stirrer at 500 rpm at ambient temperature for 24 h. To produce 4-AP-containing fibers, 4-AP (TCI America) was dissolved in 100 µL of dimethylformamide (DMF) (Carlo Erba Reagents) and incorporated in each polymeric solution. Various concentrations of 4-AP (0.02 % w/w, 0.06 % w/w and 0.1 % w/w) were tested in PCL fibers. The chosen amount of 4-AP was 0.1 % w/w for all subsequent produced membranes CS/4-AP, CS/PCL/4-AP. The solution was stirred again for 20 min to ensure even distribution of 4-AP.

2.1.2 Eletrospinning

The polymer solutions were loaded into 5 mL syringes with a 23-gauge needle tip attached, and then placed in a syringe pump (kdScientific) at a distance between the needle tip

and the collector of 23 cm. The grounded cylindrical collector to gather fibers was covered with aluminium foil and moved slow both translationally and rotationally. The flow rate of the polymeric solutions was 0.5 mL/h, and the voltage applied to the metallic needle tip ranged from 13 up to 18 kV.

2.2 Membrane Characterization

2.2.1 Scanning Electron Microscopy

Samples of each membrane were sectioned into pieces and mounted onto carbon tape that had been affixed to a metal substrate. Subsequently, a thin iridium coating was applied to all samples to allow electron emission. SEM Images were taken using a TM3030 Plus Hitachi TM 3030Plus Tabletop Microscope. The average fiber diameter was determined by analysing around 70 fibers from each image.

2.2.2 Porosity Tests

A CS solution was prepared, as previously described, and was then placed in a plate to dry. Three samples of this dry film and three samples of CS, PCL and CS/PCL membranes were cut into pieces, weighed, and measured for thickness using a digital micrometer. By determining the volume from these measurements, the apparent density of CS, PCL and CS/PCL were obtained, such as the density of CS material. The density of PCL was provided by the manufacturer (1.145 g/cm^3). The porosity was determined, where ρ is the apparent density of the membranes and ρ_0 is the material density, according to (*Porosity (%) = ((ρ_0-ρ)/ρ_0)* x *100*) [67].

2.2.3 Swelling Assays

Three samples of each membrane type, weighing approximately 20 mg, were placed in Falcon® tubes and weighed initially W_0. Following the addition of 10 mL of PBS, the samples were incubated at 37 ºC. At designated time points, the samples were removed, gently dried with filter paper, and reweighed W_w using a pre-tared weighing boat before returning them to the incubator. This process was repeated at intervals of every 30 min for the first 5 h, then hourly for the next 4 h, and finally at 24 h and 48 h. Swelling percentage was calculated using equation: (*Swelling (%) = ((W_W-.W_0)/ W_0)x100*) [68].

2.2.4 Fourier-Transform Infrared (FTIR) Spectroscopy

Samples of each membrane were analysed by Fourier-Transform Infrared (FTIR) spectroscopy. The measurements were performed using a Perkin-Elmer Spectrum Two in Attenuated Total Reflectance (ATR) mode and the transmittance spectrum was recorded across a wavenumber range of 4000 cm^{-1} to 400 cm^{-1}.

2.2.5 Drug Delivery Assay

Fibers of PCL/4-AP (1000:1), CS/4-AP(1000:1), and (CS/PCL)/4-AP(1000:1) were each cut into three pieces, with approximately 5 mg each. Additionally, PCL, CS, and CS/PCL fibers, without 4-AP, were each cut into a single 5 mg piece. These pieces were placed in separate Falcon® tubes, each containing 10 mL of PBS. Absorbance values were measured using a UV-vis spectrophotometer (ScanSpecUV, SCANSCI), with data collected via LightScan software. The wavelength used for measurements was 263 nm, corresponding to the maximum absorption of 4-AP as reported by National Institute of Standards and Technology. The measurements were performed using 2 mL of PBS from the Falcon® tubes containing 4-AP fibers, three replicates per sample, placed inside a quartz cuvette. 2 mL of PBS from the respective samples without 4-AP served as reference. After each measurement, 2mL of fresh PBS were added to the samples to maintain a constant volume. The time points were separated by 5min intervals during the first hour, and by 20 min intervals thereafter. Before and between measurements, the fibers were incubated at 37 ºC in an orbital shaker. Six concentrations (4, 6, 8,10, 12 and 15 µg/mL) of 4-AP dissolved in PBS were prepared, and their absorbance at 263 nm was measured, to get the calibration curve. This curve enabled the quantification of the 4-AP released over time.

2.2.6 Stress-strain Tests

Tensile tests were performed with a 50 N load cell at a speed of 50 mm/min at room temperature, using a TMS-Pro testing machine and Texture Lab Pro Software (Food Technology Corporation). Samples measuring (3x1) cm were prepared and their thickness was measured with a digital micrometer.

2.3 Cellular assays - In vitro evaluation

The cell lines used include a keratinocyte cell line (HaCaT, Addexbio) (San Diego, CA, USA) that are models of the main cells of the epidermis, fibroblasts cell line HFFF2 (ECACC, UK)

models of the main cells of the dermis, and human neuroblastoma cell line SH-SY5Y (CRL-2266^{TM}, ATCC, USA), as a neuronal cell model. The media utilized for cell culture was Dulbecco's Modified Eagle's Medium (DMEM)(Biowest) supplemented with 10% fetal bovine serum (FBS)(Biowest) and 1% penicillin-streptomycin (Gibco). DMEM with high glucose was used for HaCaT culture while DMEM with low glucose was used for the culture of HFFF2 and SH-SY5Y cells. In the case of 96 plate-wells, each well has an area of 0.3 cm^2 and holds 100 µL of medium, while for 24 well-plates homemade Teflon Inserts were used to hold the membranes, remaining an available area of 0.5 cm^2 and a working volume of 250 µL. Regarding cell culture, cells were cultured in a T75 flask until reaching confluence, later washed with 10 mL PBS, then treated with1 mL of Trypsin (TrypLE TM Express, Gibco) and placed in the incubator for 5min. Next, 10 mL of suplemented DMEM was added. To get the cell concentration in the cell suspension, cell counting was performed using the hemocytometer. For the resazurin assay, the cell medium was replaced with equal volumes of a resazurin solution (0.04 g/mL in PBS)(Alfa Aesar) and DMEM medium, with additional wells without cells serving as medium control. The plates were incubated for 3 h in an SANYO CO_2 incubator with 5 % CO_2 at 37 ºC, after that period wells absorbances were measured at 601 nm and 571 nm using a microplate reader Biotek ELX 800UV. Resazurin (601 nm) is reduced to fluorescent resorufin (571 nm) by metabolically active cells. The corrected absorbance (obtained by subtracting the absorbance measured at 601 nm to the absorbance at 571 nm and subtracting the medium control) is proportional to cell viability.

2.3.1 Cytotoxicity Assays

The cell types used in the cytotoxicity test of 4-AP included HaCaT, HFFF2 and SH-SY5Y cells. For each test, cells were seeded in a 96-well plate at a density of 30000 cells/cm^2 for SH-SY5Y and 25000 cells/cm^2 for HaCaT and HFFF2. The plates were incubated for 24 h in DMEM, then the medium was replaced with DMEM containing 4-AP. The 4-AP concentration, starting at 16 mM, was progressively reduced through successive dilutions by a factor of 2 until reached 0.063 mM. In the negative control, complete DMEM was used, while in the positive control, 10 % Dimethylsulfoxide (DMSO) with DMEM was used. The plate was incubated for 48 h in 5 % CO_2 at 37 ºC. To assess cell viability, a resazurin assay was performed, as described in previous section.

2.3.2 Adhesion and Proliferation Assays

Cell adhesion and proliferation assays were conducted using HFFF2 and HaCaT cells. Membranes were cut into 12 mm disks, sterilized with UV light for 2 h on each side, and placed in a 24-well plate inside Teflon inserts. 5 replicates per membrane were used. Membranes were washed with PBS and then with complete culture medium. Cells were seeded in the membranes, and in glass coverslips (placed inside the Teflon inserts), which served as the cell controls, at a density of 25000 cells/cm^2 for both cell lines. Cells were incubated in 5 % CO_2 at 37 ºC. Resazurin assays were conducted on days 1, 4, 7, 10, and 14 after cell seeding. On the 7th day, one replicate of each membrane was fixed to analyse cell morphology. To do that, cells were washed three times with PBS for 5 min each, then fixed with 4 % paraformaldehyde for 20 min and washed again three times with PBS. To permeabilize the cells, Triton X-100 (0,1% in PBS) was applied for 5 min, after which the cells were washed once more with PBS. Cell cytoskeleton were stained with phalloidin 488 (in 1% bovine serum albumine) and maintained in the dark for 90 min, followed by another wash with PBS. The nucleus was subsequently stained with 4',6-diamidino-2-phenylindole (DAPI 300, Thermo Fisher, Waltham, MA, USA) (in PBS) for 5 min, and washed again three times with PBS, followed by two washes with water for 5 min each. Finally, the samples were placed on glass coverslips with a drop of Mowiol mounting media (Sigma-Aldrich) and stored overnight at 4 °C in the dark. Visualization of the samples was performed using an epi-fluorescence microscope (Nikon Eclipse Ti-S), equipped with a Nikon D610 digital camera.

2.3.3 Wound Healing Assays

The assay involves creating a gap in a layer of cells to mimic a wound. To create these consistent gaps, a 4 well silicone insert (ibidi®), featuring defined (500 ± 100) µm cell-free gaps, was placed in a 12-well plate. These silicone inserts have a sticky underside that ensures they adhere securely in the plate well. Two tests were conducted, one with HFFF2 cells and the other with HaCaT cells. Cells were seeded into the holes of the inserts at a density of 25000 cells/cm^2 with a volume of 100 µL per hole. The plates were incubated at 37 °C in a humidified atmosphere containing 5 % CO_2. Cell growth was monitored until confluence was reached, approximately 48h later. Afterwards, the inserts were removed from the wells using sterilized forceps. The wells were washed once with PBS and were treated with 4-AP at three concentrations: 1 mM, 0.5 mM, and 0.25 mM. A control well was filled with complete media. Subsequently, images were captured using an optical microscope for every 6h to monitor cellular migration and

proliferation until the gap was closed. The 4-AP and the medium in the wells with the same initial conditions were changed throughout the experiment when necessary. The images were analysed to quantify cellular migration using the ImageJ/Fiji® plugin known as *Wound Healing Size Tool* [69]. The percentage of wound closure was calculated according to (*Wound Closure (%) =* $((A_{t=0} - A_{t=\Delta t})/A_{t=0})x100$) [69]. Let $A_{t=0}$ represent the initial wound area, and $A_{t=\Delta t}$ the wound area at n hours post-scratch, both measured in μm^2 [69] .Considering W_i is the mean initial wound width, and W_f is the mean final wound width, both in μm, and t represents the assay duration in hours [69], the rate of cell migration was determined by the equation: (*rate of cell migration (%) =*$((W_i - W_f)/t)x100$) [69].

2.4 Neurite Outgrowth Assays

Membranes were cut into 12 mm disks, sterilized with UV light for 2h on each side, and placed in 24-well plates inside Teflon inserts. Membranes were washed with PBS, then with culture medium. SH-SY5Y cells were seeded onto the membranes and onto 12 mm glass coverslips, at a density of 4000 cells/cm^2. After 24h of incubation in complete DMEM, four samples of each membrane and two controls were treated with medium containing retinoic acid (RA) (Sigma Aldrich). RA was prepared in DMSO (10 mM) and diluted in the medium solution: DMEM with 3% FBS and 1% penicillin/streptomycin (P/S) to a final concentration of 10 μM. Other four samples and two controls were treated with the prior medium solution, while four coverslips were treated with 0.5 mM of 4-AP in the earlier medium solution, two of them also received 10 μM RA. Media were changed every 48h for 12 days. Afterwards, cells were fixed as previously described. Staining began 24h later, with membranes washed, permeabilized with Triton X-100 (0.3% in PBS) for 5min, and incubated, after PBS washes, with 5% BSA (Biowest) in PBS for 1h. Primary antibodies, β-tubulin (Cell Signaling Technology) (1:200) and Microtubule-Associated Protein 2 (MAP-2) (Invitrogen) (1:300) dissolved in 1% BSA, were added and incubated overnight at 4°C. In PBS-washed membranes, secondary antibodies were applied Alexa Fluor™ 488 goat-conjugated anti-rabbit IgG (Invitrogen) (1:1000) for β-tubulin and Alexa Fluor™ 488 goat-conjugated anti-mouse IgG (Invitrogen) (1:1000) for MAP-2, along with Phalloidin-IFluor™ 555 (Cayman Chemical Company)(1:1000) diluted in 1% BSA, in the dark for 2h, later washed with PBS. Controls were treated with only secondary antibodies to ensure primary antibody specificity. DAPI (10 μM) in PBS, was applied to all samples for 5min, followed by PBS and water washes. Samples montage and imaging occurred as previously described in the adhesion and proliferation assay.

3

RESULTS AND DISCUSSION

3.1 Membranes characterization

3.1.1 Morphology through Scanning Electron Microscopy

SEM images and corresponding average fiber diameter distributions of PCL, CS and CS/PCL membranes were obtained. In Figure 7, the morphology of the PCL membranes with varying amounts of 4-AP (0.02 % w/w, 0.06 % w/w and 0.1 % w/w), as well as the pure PCL membrane without 4-AP was observed.

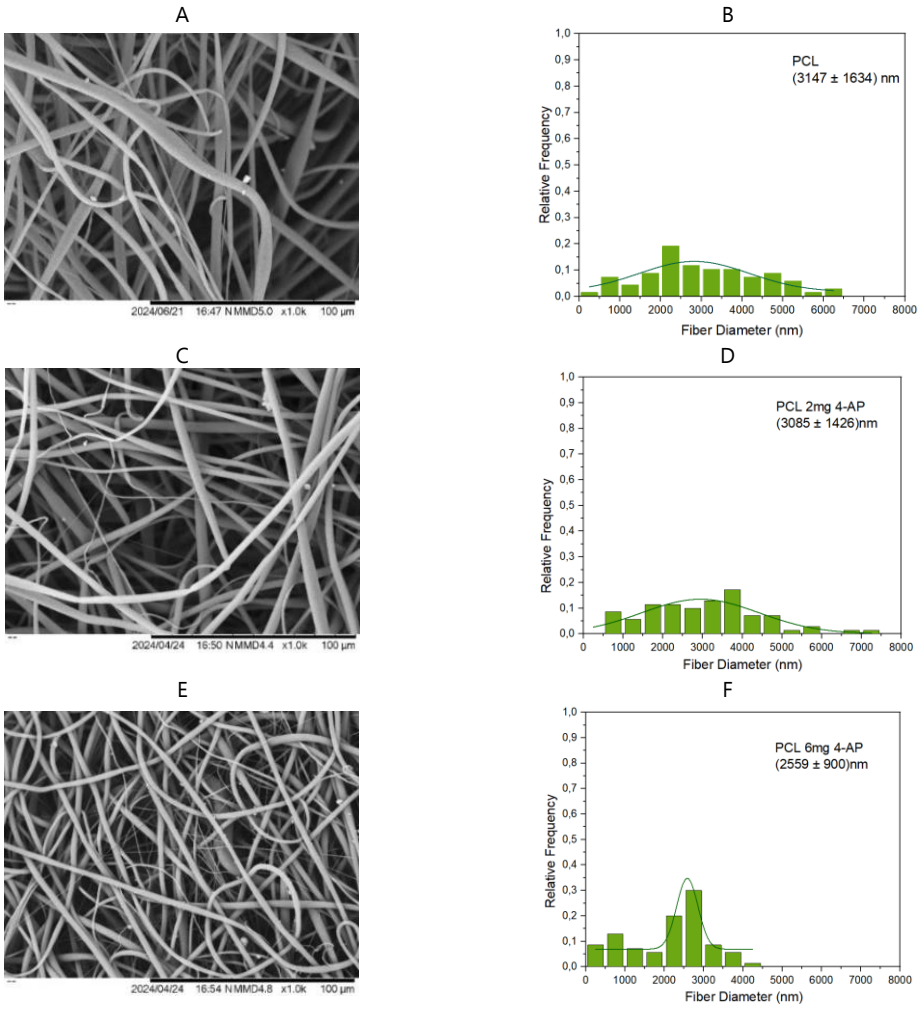

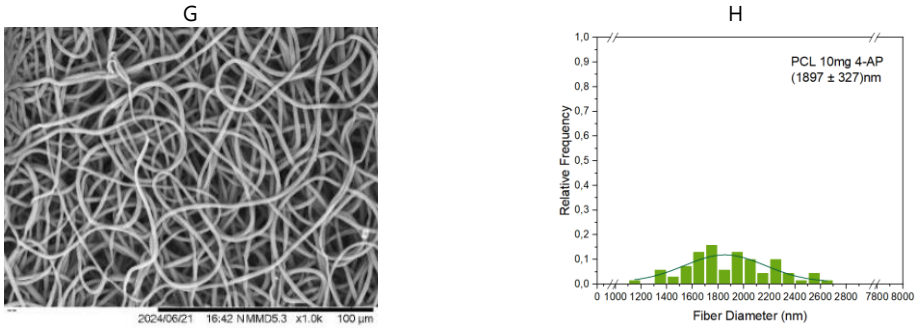

Figure 7-(A)PCL. (B)PCL histogram. (C) PCL/4-AP (5000:1) (D) PCL/4-AP (5000:1) histogram. (E) PCL/4-AP (1667:1) (F) PCL/4-AP (1667:1) histogram. (G) PCL/4-AP (1000:1). (H) PCL/4-AP (1000:1) histogram.

Figures 8 and 9 present the structure of CS, CS/4-AP (1000:1), CS/PCL and (CS/PCL)/4-AP(1000:1). These confirmed the feasibility of electrospinning of PCL, CS and CS/PCL containing 4-AP. The fibers appear as a continuous structure, without significant defects. The fibers are randomly orientated, creating interconnected pores within the membrane. CS and PCL nanofibrous scaffolds, Figure 7A and 8A, are characterized by an arrangement of extremely fine, interconnected fibers that form a three-dimensional network. Other researchers obtained similar morphology for CS [67], [70], [71] and for PCL [67], [70], [53].

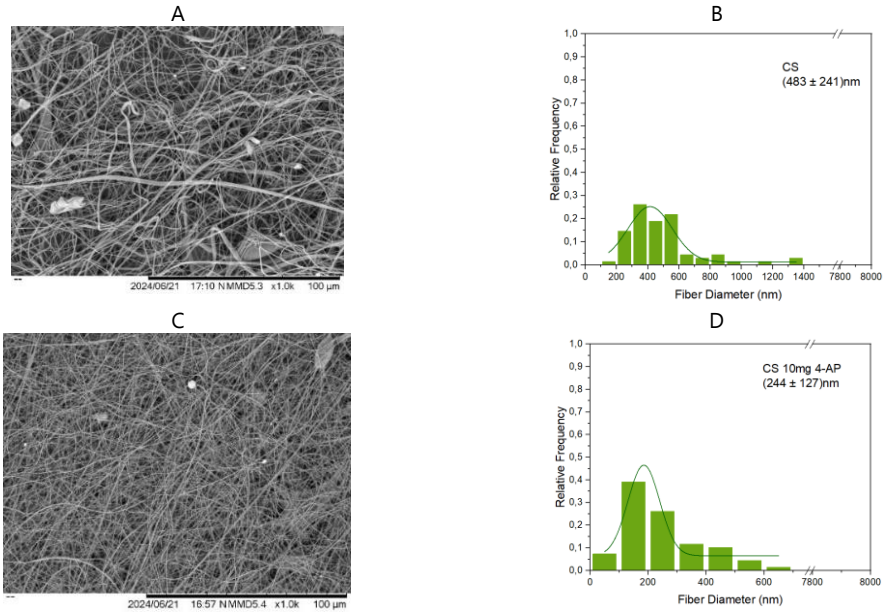

Figure 8 -(A) CS. (B) CS histogram. (C) CS/4-AP (1000:1) (D) CS/4-AP(1000:1) histogram.

The presence of 4-AP did not affect the fibers morphology, resulting in membranes with a porous configuration suitable for applications in skin TE, as it provides an ideal environment for cell adhesion and proliferation, while facilitating the exchange of nutrients and metabolic waste. The fiber diameters of CS and PCL differ significantly due to the properties of their solutions. CS, being highly conductive, forms thinner fibers, averaging 483 ± 241 nm, while PCL

fibers, dissolved in chloroform, are much thicker, averaging 3147 ± 1634 nm. These results are consistent with previous studies by Lungu *et al.* [71] for CS fibers and Khan *et al.* [53] for PCL fibers.

The results revealed that the fiber diameter is influenced by the presence of 4-AP, since average fiber diameter decreased as the 4-AP content increased, under the same experimental conditions.

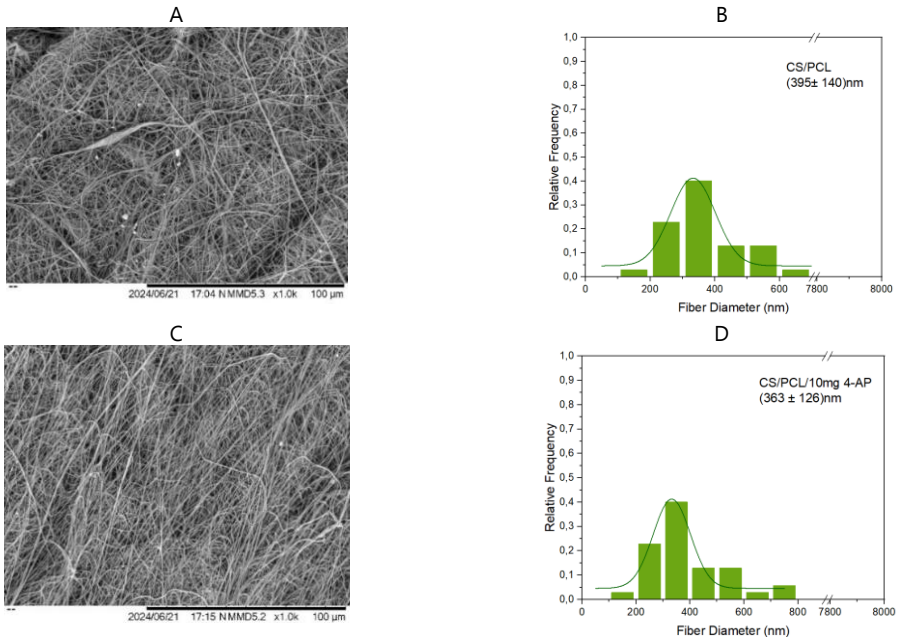

Figure 9-(A) CS/PCL. (B) CS/PCL histogram. (C) (CS/PCL)/4-AP(1000:1) (D) (CS/PCL)/4-AP(1000:1) histogram.

Measurements of PCL showing average fibers diameter of 3085 ± 1426 nm for PCL/4-AP (5000:1), 2559 ± 900 nm PCL/4-AP (1667:1), and 1897 ± 327 nm for PCL/4-AP (1000:1), compared to 3147 ± 1634 nm for simple PCL fibers. Average values of 483 ± 241 nm for CS fibers, and 244 ± 127 nm for CS/4-AP (1000:1). However, this effect of 4-AP is minimal in the CS/PCL fibers, average fiber diameters for CS/PCL and (CS/PCL)/4-AP(1000:1) were 395 ± 140 nm and 363 ± 126 nm, respectively. The average fiber diameters for PCL, CS and CS/PCL scaffolds, were consistently within diameters ranging from nanometers to micrometers.

Across all tested 4-AP concentrations bead-free nanofibers were more prominent in PCL/4-AP (1000:1) composition. Additionally, the fiber diameters were smaller with this quantity of 4-AP, making it more favourable to the formation of nanofibers. Given that the daily oral dose of 4-AP for human treatment ranges between 10 and 30 mg [63], the membranes used in all subsequent tests in this dissertation were produced with 0.1 % w/w 4-AP, in the development of this system for local drug application.

3.1.2 Porosity Tests

PCL ρ_0 provided is 1.145 g/cm^3. The ρ_0 determined from a film produced from the CS polymeric solution was 0.766 g/cm^3. ρ_0 obtained for CS/PCL was 0.918 g/cm^3; while the ρ obtained is presented in table 3.1.

Table 3.1- Results of apparent density (ρ) of the membranes.

	PCL	PCL/4-AP	CS	CS /4-AP	CS/PCL	CS/PCL /4-AP
ρ (g/cm^3)	0.289	0.191	0.204	0.171	0.178	0.208

The membranes demonstrated significant porosity, Figure 10, with values of approximately 80%. PCL/4-AP membranes exhibited the highest porosity, exceeding 80%. There was no significant difference in overall membrane porosity. However, PCL membranes exhibited higher porosity than CS membranes, with both being lower than that of the CS/PCL composite membranes. Kao *et al.* also reported that the porosity of PCL membranes was lower than the CS/PCL composite membranes [72]. Lim *et al.* obtained porosity values of the same order of magnitude for PCL membranes [73]. The incorporation of 4-AP into the fibers affected porosity, leading to an increase of porosity in PCL and CS membranes, while causing a slight decrease in the composite matrix.

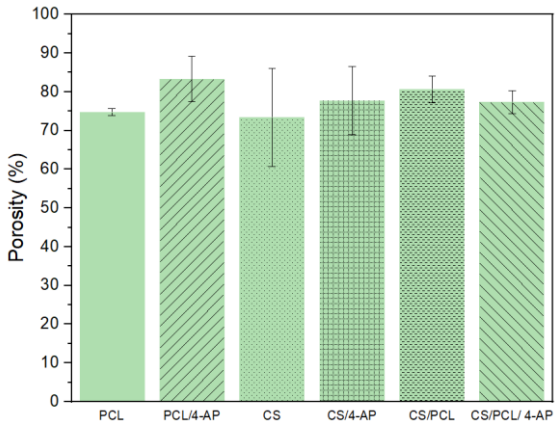

Figure 10- Porosity of membranes (n=3; mean ± SD).

These results indicate that the membranes exhibit similar porosity levels. This high porosity, which emphasizes the interconnectivity of the pore networks, makes the fibers excellent candidates for cell attachment and facilitates the transport of nutrients and oxygen.

3.1.3 Swelling of Membranes

Swelling is defined as the expansion of a solid due to fluid absorption, driven by equilibrium restoration, with pressure increasing initially but slowing as equilibrium is approached.

The swelling behaviour of the CS, PCL, CS/PCL, CS/4-AP, PCL/4-AP, and CS/PCL/4-AP membranes was evaluated, and the results are presented in Figure 11, to characterize their capacity to absorb PBS. PCL-based membranes, exhibit a swelling rate profile with a sharp increase within the first 120 minutes, followed by alternating increases and decreases until reaching equilibrium at around 400 minutes, with a rate constant between 300% and 350%. Whereas the initial oscillation between swelling and deswelling exhibited a smaller amplitude in the CS and CS/PCL membranes up to approximately 200 minutes.

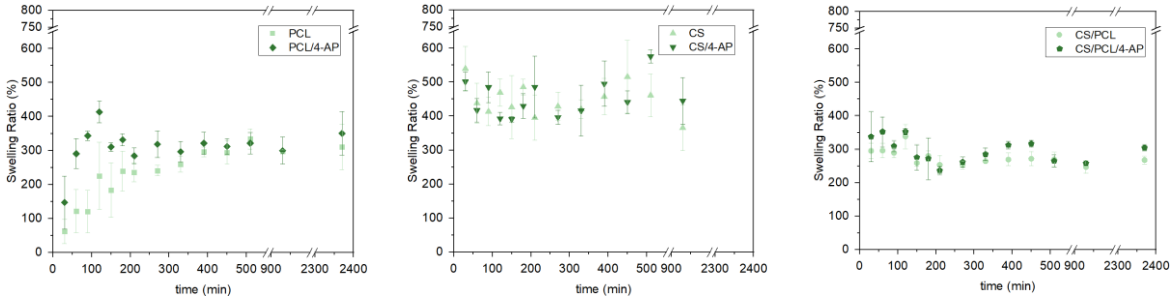

Figure 11- Swelling ratio for PCL, PCL/4-AP, CS, CS/4-AP, CS/PCL, CS/PCL/4-AP scaffolds. (n=3; mean ± SD).

The study highlighted the hydrophilic nature of CS significantly contributes to its superior swelling capacity, as it absorbs water, whereas PCL, being a hydrophobic polymer, does not exhibit water absorption. CS-based membranes exhibited the highest swelling rates, with values of (539.61±64.82) %, (469.33±40.41) %, (485.34±23.58) % and (515.59 ±107.29) % for CS at 30, 120, 180 and 450 minutes respectively; and for CS/4-AP (501.42±27.31) %, (485.53±91.35) %, (495.28±66.67) % and (575.75 ±196.84) % at 30, 210, 390 and 510 minutes respectively. Poddar *et al.* [74], also observed higher swelling rates for CS compared to PCL. Contrary to what was mentioned by Gupta *et al.* [75], who associated the elevated swelling rate of polymers with high porosity and pore interconnection, in the present study, the PCL fibers with greater porosity exhibited less swelling. 4-AP seemed to enhance swelling functions of the membranes, mainly CS/PCL/4-AP and PCL/4-AP compared to CS/PCL and PCL respectively.

Liquid absorption capacity is a key factor in enhancing drug delivery potential in polymeric systems. When in contact with physiological fluids, the carrier swells, causing disintegration and drug release [28]. This indicates that the higher swelling capacity of CS, improves drug release in liquid environments compared to PCL nanofibers. However, excessive swelling may reduce mechanical stability [68], suggesting that CS/PCL membranes could be an effective solution for 4-AP delivery. Optimizing the relative proportion of CS to PCL is necessary for controlled drug release.

3.1.4 Fourier-Transform Infrared (FTIR) Spectroscopy

The chemical structure of the membranes was determined using FTIR. The FTIR spectra of all membranes is shown in Figure 12. Reading the FTIR spectrum of PCL membranes obtained, the most prominent peaks include the C=O stretching of the carbonyl group at 1720 cm^{-1} and the C-H stretching vibrations of aliphatic methylene groups (-CH_2-) observed in a double peak at 2870 and 2950 cm^{-1}. Additionally, the C-O-C stretching, indicative of ester linkages, appears within the range of 1160–1240 cm^{-1}. Methylene bending vibrations are identified at 1470 cm^{-1}, corresponding to C-H bending. These values are consistent with the molecular structure of PCL, Figure 4. Phillipson *et. al* presented measurements that align with the expected range for the identified chemical functional groups in PCL [76].

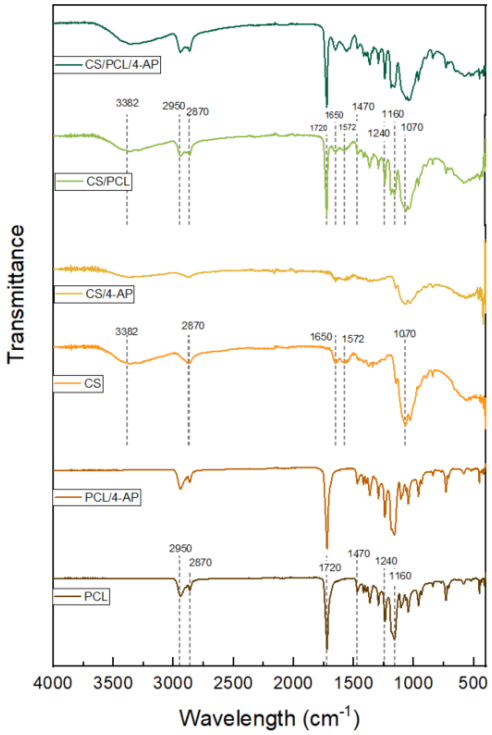

Figure 12- Transmittance FTIR Spectra for PCL, PCL/4-AP, CS, CS/4-AP, CS/PCL, CS/PCL/4-AP scaffolds.

Regarding the CS FTIR spectra, in Figure 12, the broad and intense peak observed at 3382 cm^{-1} is associated with the stretching vibrations of O-H and N-H bonds, indicative of hydroxyl and amine groups. The C-H stretching vibrations of aliphatic methylene groups appear at 2870 cm^{-1}. A distinct peak at 1650 cm^{-1} corresponds to the C=O stretching from the partial deacetylation of chitosan, while the N-H bending vibrations is found at 1572 cm^{-1}. Additionally, the C-O-C stretching vibrations are observed at 1070 cm^{-1}. Pieklarz *et. al* reported values that fall within the specified range for the mentioned chemical functional groups. [77]. As expected, in the case of the CS/PCL membranes, the absorption band corresponding to PCL remains present

with an overlap of the characteristic bands of CS. FTIR analysis showed no significant peaks for 4-AP due to its low concentration compared to the membrane materials concentration. However, CS/4-AP membrane signals were more attenuated than CS membrane, indicating possible molecular interactions between CS and 4-AP.

3.1.5 Drug Delivery Assay

The drug delivery assay enables the study of the release behaviour of 4-AP incorporated into the membranes. The absorbance values measured were related to the calibration curve, enabling the quantification of the cumulative mass throughout the assay. Figure 13 represents plots of the cumulative 4-AP mass as a function of time, for PCL, CS and CS/PCL.

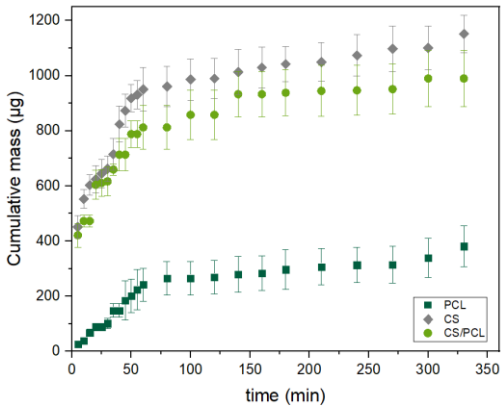

Figure 13- Release profile of 4-AP from PCL, CS and CS/PCL samples into PBS. Three replicates were assembled for each sample type. Plotted values represent mean ± SD.

The results indicate that the released concentration of 4-AP exhibits an abrupt increasing trend during the first 50 minutes of testing for CS membranes, 80 minutes for PCL and 140 minutes for CS/PCL membranes. From then onwards the release is very smooth extending up to 330 minutes, as seen on the graph in Figure 13. All membranes exhibit two steps release profile, with an initial burst release followed by a controlled release. The release profile of 4-AP from the electrospun membranes varied depending on the polymer used [78]. After 50min CS presents a cumulative mass release of 918 µg, PCL reveals 202 µg and CS/PCL shows 788 µg of mass released. An ideal sustained-release device should release the drug at a rate sufficient to maintain an effective dose in plasma concentration over an extended period. This ensures consistent therapeutic effects and minimizes the frequency of dosing. The choice of the polymers can significantly influence the release kinetics, thereby affecting the duration and efficacy of the drug's action. Analysis of the 4-AP release profile from the produced membranes, revealed that in PCL membranes a substantially smaller quantity of 4-AP was released in the first

300 minutes, 381 µg, compared to both CS and CS/PCL membranes. Followed by CS/PCL, which lead to less quantity, 990 µg, than CS membranes, 1152 µg. This suggests that the increased release may be because of the higher swelling capacity of CS, which promotes molecule release in a liquid environment, in contrast with the PCL nanofibrous scaffold used in this study. The increase may also be related to CS higher degradation rate. Prabaharan *et al.* [79] indicated that drug release from natural polymers typically occurs quickly due to their decomposition within a few hours, whereas synthetic polymers provide prolonged release, as they can resist degradation in the body for several days or even weeks, which is in line with what was observed in this study.

The 4-AP release data were fitted to various kinetic models including zero-order [80], Higuchi [81], first-order [82], Korsemeyer–Peppas [83], and Hixson–Crowell [31] equations. To adjust the experimental data to the theoretical models, a linear fit of the data was applied to plot the results as:

Zero order	Q(t) versus t
Higuchi	Q(t) versus $t^{1/2}$
First order	log Q(t) versus t
Korsmeymer-Peppas	log %Q(t) versus log %t
Hixson–Crowell	Q(t) versus $t^{1/3}$

Where the amount of 4-AP released at time t, is denoted as Q(t). The selection of the most appropriate kinetic model for describing the drug release data was based on square of correlation coefficient (R^2). CS/PCL (R^2=0.9783) and PCL (R^2=0.9609) membranes correlation coefficients indicated a higher correlation in Higuchi release kinetics compared to other models, as observed in Table 3.2. This suggests that the predominant 4-AP release mechanism of the CS/PCL and PCL membranes provides a consistent rate of drug release over time, allowing for controlled-release. The Higuchi equation describes drug release from structures where the drug is homogeneously dispersed [31]. This model considers not only the transport of the drug from the center of the matrix but also includes drug dissolution processes [84], [85], [30], provides important insights into the release phenomena from matrix systems [31].

Table 3.2- Results of Model Fitting for 4-AP (R^2 (square of correlation coefficient)).

Model	Zero order	Higuchi	First order	Kors-Peppas	Hixson–Crowell
	R^2	R^2	R^2	R^2	R^2
PCL	0.7625	0.9609	0.9009	0.9016	0.8535
CS	0.9683	0.9504	0.9684	0.9327	0.9684
CS/PCL	0.9647	0.9783	0.9651	0.971	0.9649

The drug release process generally involves multiple mechanisms, with one typically being predominant. However, in the case of CS membranes, the available data do not clearly

indicate a dominant mechanism. In this study 4-AP release lead to coefficients that are similar across various models, Zero order, First order and Hixson.

The release mechanisms of a drug are influenced not only by the structure of the drug but also by the shape and chemical composition of the polymer. Studies on the release of various drugs from CS nanoparticles have identified various models, such as the Higuchi model for Ganciclovir (Patel *et al.* [86]), the Korsmeyer-Peppas model for Diltiazem hydrochloride when carrier is L-leucine conjugated CS (Muhsin *et al.* [87]) and Lovastatin from CS/alginate (Thai *et al.* [88]), and the zero-order model for Diosgenin monoesters using steroid–CS conjugates (Quinones *et al.* [89]).

Current efforts focus on achieving long-term drug release, though excessive release can diminish therapeutic effectiveness [84]. Consequently, recent research has explored pulsatile or stimulus-responsive drug delivery systems [85], [90], with pH variation being a potential solution to achieving this goal.

3.1.6 Stress-strain Tests

A stress-strain curve representative of the mechanical behaviour of each membrane is shown in Figure 14.

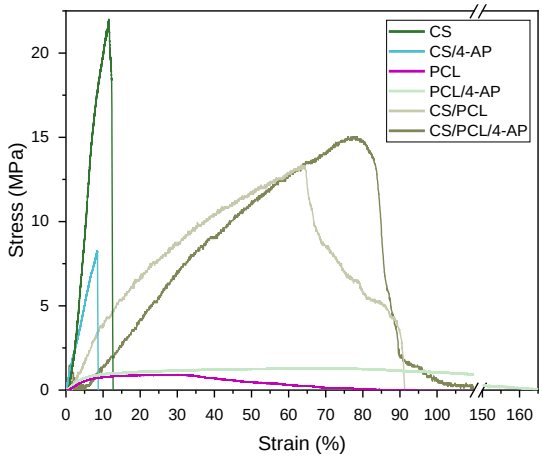

Figure 14- CS, CS/4-AP, PCL, PCL/4-AP, CS/PCL, CS/PCL/4-AP stress strain curves.

The analysis of the stress-strain curves for six fiber types reveals distinct mechanical behaviours. Both PCL and PCL/4-AP exhibit mainly elastic phases. CS/4-AP displays an elastic phase up to 8.39% strain, while CS extends this phase to 11.52% strain. In contrast, the CS/PCL fibers demonstrate a significant elastic phase, enduring up to 63.25% strain. Notably, CS/PCL/4-AP fibers show the most remarkable performance, maintaining their elastic phase up to 75.92% strain. These findings highlight the enhanced mechanical properties of the CS/PCL blends, particularly with the incorporation of 4-AP, suggesting their potential for applications

requiring higher deformation capacity. Scaffold materials for soft tissues should exhibit reversible deformation while maintaining a high degree of recoverability, which refers to their ability to undergo elastic deformation [91]. Young's modulus was calculated from the slope of the linear region in the stress–strain curve, the values are represented in Table 3.3. Vieira *et. al* found similar values to CS young's modulus [67], although PCL values in the present study appeared different. This difference might be explained by the humidity conditions in which membranes were produced.

Table 3.3- Results of Young's modulus of electrospun fibrous membranes.

	PCL	PCL/4-AP	CS	CS /4-AP	CS/PCL	CS/PCL /4-AP
Young Modulus (MPa/%)	0.1	0.2	1.7	1.1	0.4	0.3
Elongation at break (%)	26.68	68.33	11.52	8.39	63.25	75.92
Tension at break (MPa)	0.91	1.32	22	8.25	13.33	15.02

3.1.7 Cytotoxicity Assays

The cytotoxicity of the 4-AP was evaluated using HFFF2, HaCaT, and SH-SY5Y and the results are presented in Figure 15.

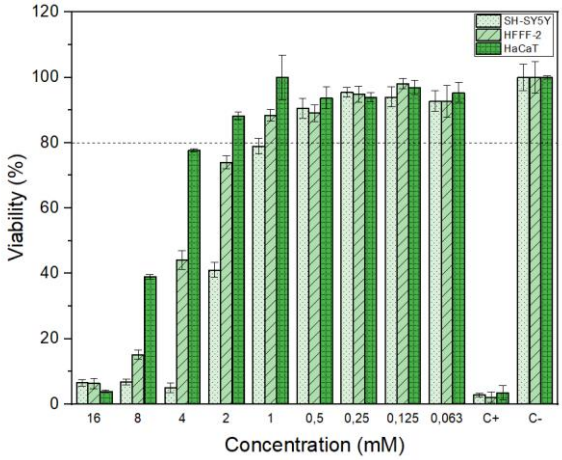

Figure 15- Cytotoxic assay of 4-AP for HFFF2, HaCat and SH-SY5Y. (n=4) Mean±SD.

Concentrations of 4-AP resulting in cell viability above 80 % are considered non-cytotoxic. Low cell viability values for the positive control and high values for the negative control confirmed the accuracy of the tests. Analysing the cytotoxicity data of 4-AP on HFFF2, it was observed that concentrations of 16 mM, 8 mM and 4 mM exhibited highly cytotoxic effects, while the threshold for non-cytotoxic concentrations starts at 1 mM of 4-AP. In HaCaT cells exposed to 4-AP for 48 h, the 16 mM and 8 mM concentrations exhibited highly cytotoxic effects, with non-cytotoxic effects observed above 2 mM. For SH-SY5Y, concentrations of 16

mM, 8 mM, 4 mM, and 2 mM showed significant cytotoxicity, while non-cytotoxic concentrations were identified starting at 0.5 mM. The SH-SY5Y cells are highly sensitive [92], to external compounds and are prone to significant reductions in viability when exposed to higher concentrations of 4-AP.

3.1.8 Adhesion and Proliferation Assays

To evaluate the impact of electrospun fibers, both with and without 0.1 % w/w 4-AP, on biological systems, HFFF2 and HaCaT cells were cultured on the fiber mats for up to 14 days. The resazurin assay was used to assess the biocompatibility of the fibers in cell culture, with the results presented in Figure 16. This assay allowed for the quantification of cell viability, and metabolic activity providing insights into the ability of the fibers to support cellular growth and proliferation over the incubation period.

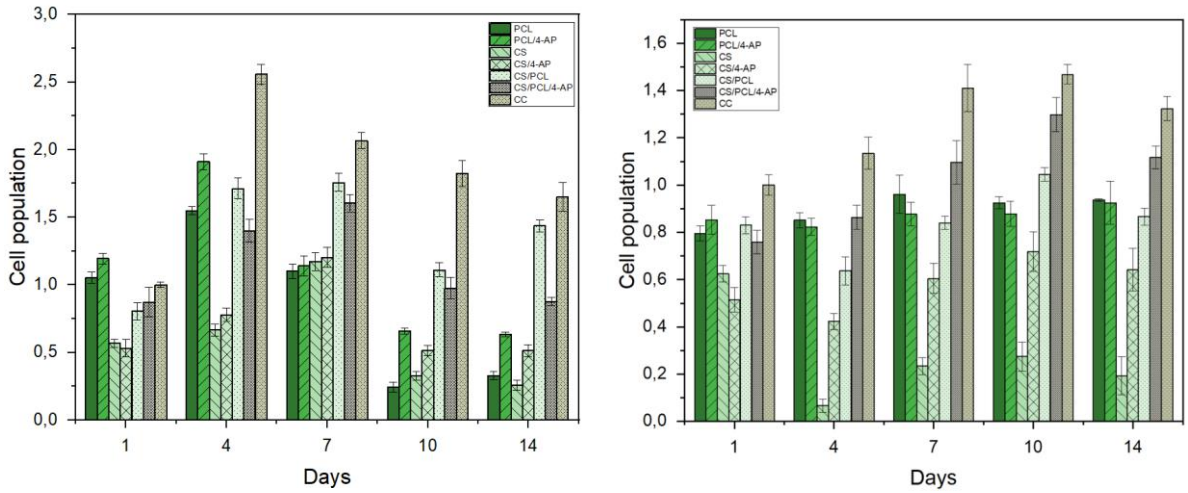

Figure 16- Cell population of HFFF2 (A) and HaCaT (B) seeded on the surface of the membranes and on tissue culture wells (CC) (n=6) Mean±SD.

On day 1, PCL/4-AP membranes exhibited the highest adhesion rate for HaCaT cells, followed by CS/PCL, with both showing over 80% adhesion compared to the control. For HFFF2 cells, PCL/4-AP membranes also demonstrated superior adhesion, indicating that a large part of the seeded cells adhered well to this membrane. The lowest adhesion values for both cell types were observed on CS and CS/4-AP membranes. These low adhesion rates observed in the CS membranes suggest that the cells may have encountered insufficient anchoring sites, resulting to reduced cell survival. Querido *et al.* [64] also obtained low values for adhesion and proliferation of HFFF2 on CS membranes compared to PCL. On day 4, both cell populations were reduced on the CS membranes, followed by the CS/4-AP group. The highest cell

proliferation was observed in HaCaT cells cultured on CS/PCL/4-AP, while HFFF2 cells showed optimal growth on PCL/4-AP membranes, which indicate that, in these cases, an adequate number of cell-fiber adhesions were formed after seeding. This trend persisted for HaCaT cells, on days 7, 10, and 14 throughout the culture period. For HaCaT cells, on day 7, PCL-based membranes show higher viability, while CS membranes exhibit a lower cell population, with an increase observed in the presence of 4-AP. On day 7, the viability of HFFF2 cells appears similar across the PCL, PCL/4-AP, CS, and CS/4-AP groups. However, CS/PCL and CS/PCL/4-AP membranes exhibit higher number of cells, with the addition of 4-AP slightly reducing these values. It was found that the presence of 4-AP increased cell proliferation in PCL and CS membranes when compared with the fibers without 4-AP, but in CS/PCL membranes this increase was observed on day 1 and on subsequent days a slight decrease was observed only for HFFF2 cells.

Fluorescence microscopy images were obtained to observe the morphology of the cells on the membranes. The cells seeded in the membranes were stained with DAPI for nucleus, in blue, and with F-actin, a cytoskeletal protein, labelled in green. The images were obtained after 7 days of culture and are presented in Figure 17 for HaCaT and Figure 18 for HFFF2.

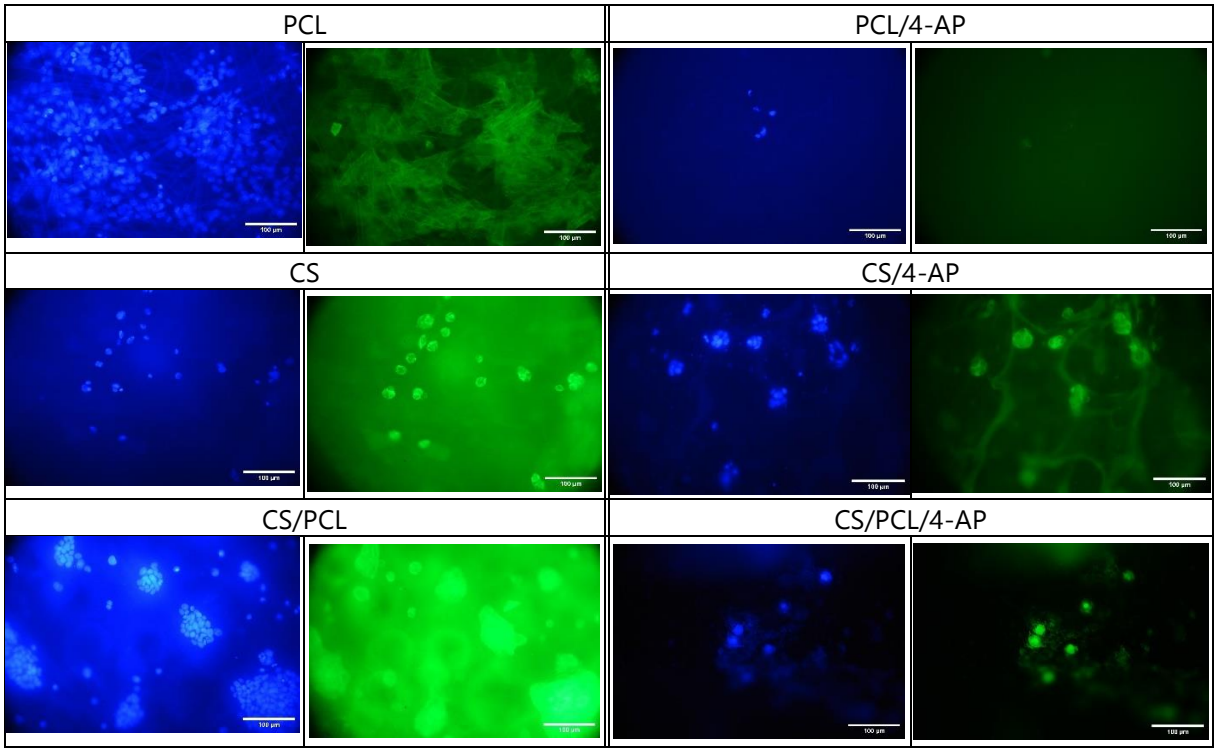

Figure 17- Fluorescence images of HaCaT cells in the membranes. Samples were marked with DAPI and Phalloidin. Scale bar: 100 µm.

In HaCaT cells, CS/PCL/4-AP membranes appear to support a higher cell population based on quantitative measurements. However, microscopic observations indicate that PCL membranes may contain a greater number of cells either HFFF2 or HaCaT. In PCL fibers, both

HFFF2 and HaCaT cells can be clearly observed adhering to the membranes, with their spatial distribution visible in the fibrous structure. The cells are widely spread throughout the fibers, indicative of a favourable environment for cell growth.

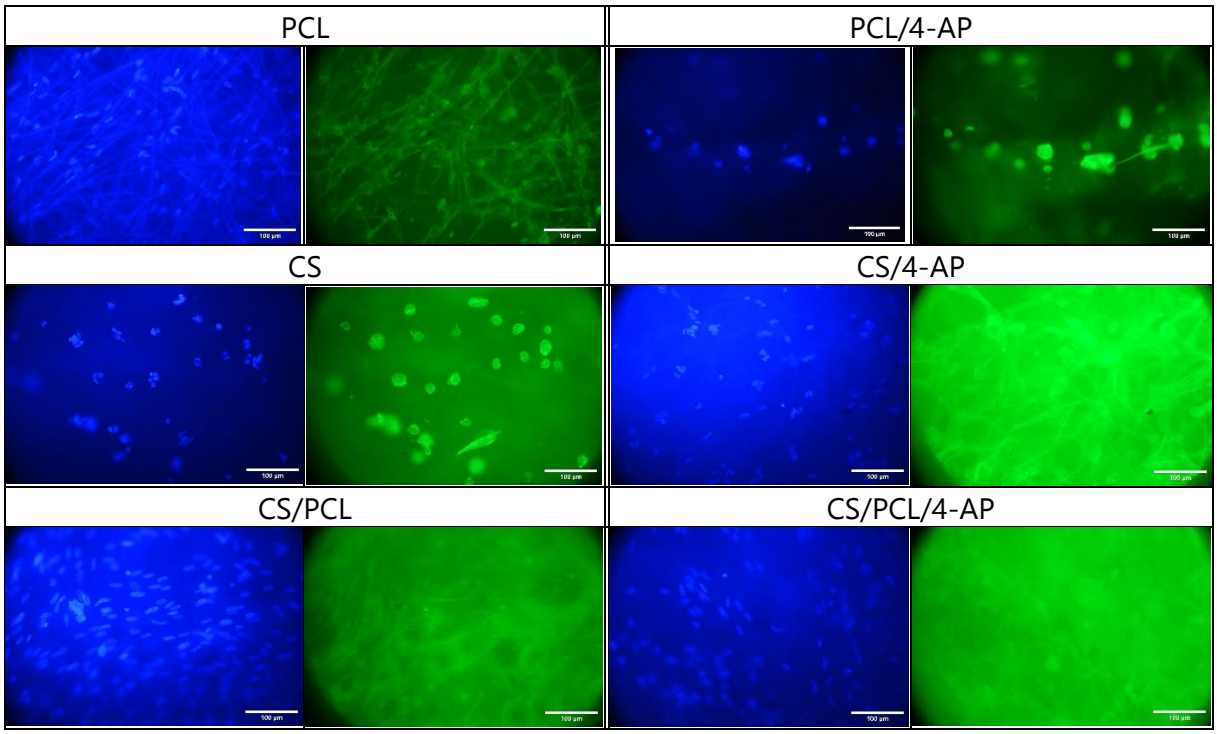

Figure 18- Fluorescence images of HFFF2 cells in the membranes. Samples were marked with DAPI and Phalloidin. Scale bar: 100 µm.

The inclusion of 4-AP in PCL fibers appears to reduce cell population, as observed in the microscopy images for both cell lines, observed by the reduction of the number of nuclei, which was in accordance to the reduced cell population seen in quantitative measurements. Similarly, in both HFFF2 and HaCaT cells, CS membranes show a lower cell population when compared to the PCL membranes. The cells are growing in clusters, presenting a less stretched morphology indicating that the surface characteristics of the CS membranes may be less conducive to supporting widespread cell adhesion and proliferation. Gomes *et. al* also found these clusters in CS membranes suggesting that is due to motile cells [70]. The morphology of the cells was not changed with the presence of 4-AP in the CS membranes. For HFFF2 cells, CS/PCL membranes exhibit a higher cell population, as confirmed by the higher number of nuclei, which reveals enhanced cell attachment and distribution. In these membranes, HFFF2 cells are distributed throughout the membrane while HaCaT cells appear in aggregates, suggesting cellular responses to the composite membrane's surface. CS results align well with resazurin values, showing similar outcomes for CS and CS/4-AP in HFFF2 cells, with an increased cell count in CS/4-AP. However, significant discrepancies occur with PCL and CS/PCL, where the addition of

4-AP leads to a marked reduction in cell numbers, visible under fluorescence but not in resazurin assays. This suggests a harmful interaction between PCL and 4-AP, though the lack of corresponding effects in resazurin is puzzling. To clarify these findings, further proliferation assays using alternatives like MTS or WST are recommended, along with DNA quantification via the PicoGreen assay to investigate potential cell death linked to the PCL-4-AP interaction. Additionally, the excessively thin membranes may have hindered cell visualization and analysis.

3.1.9 Wound Healing Assay

The wound healing assay, an *in vitro* technique, allows investigating collective cell migration in two dimensions. To investigate cell migration in the presence of 4-AP, the HaCaT and HFFF2 cell lines were employed in this wound healing study as they are key components of the skin and possess biological characteristics that mimic essential processes involved in tissue repair. The inserts utilized allow for a fixed wound size and do not damage the surface or the cells, unlike the traditional scratch assay. The cell-free zone created in this assay induces the remaining cells to migrate into the gap. Optical microscopy images were taken at regular intervals of time throughout the experiments to assess the impact of 4-AP on cell migration. As illustrated in the image sequence shown in Figure 19, HaCaT cells maintain contact while migrating in a directed and coordinated manner toward the wound area from 0 h to 48 h, with the gap depicted corresponding control well.

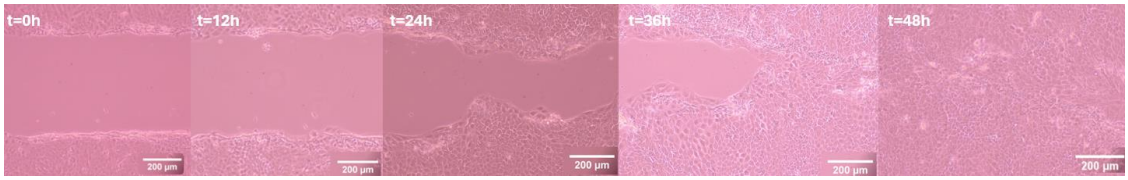

Figure 19- Micrograph of wound healing assay, from the control well of HaCaT cells in 5 different time points. Scale bar: 200 µm.

Initially, 4-AP concentrations starting at 2 mM were used; however, the results were not satisfactory, which is consistent with the cytotoxicity assays. Consequently, the concentrations were adjusted and concentrations of 1 mM, 0.5 mM, and 0.25 mM were used. Cell migration can be evaluated by measuring the distance or area of the wounded region devoid of cells. To obtain these values, an ImageJ/Fiji® plugin [69] was used to analyse 336 images. An image for each section of each well was captured at specific time points to obtain an average value per well. To examine the microscope images, the files were first exported in JPG format. Afterward, they were opened using ImageJ software, where the distance measurement units were converted from pixels to micrometers. This scaling adjustment was applied uniformly to all images

before proceeding with the analysis. The plugin enables the quantification of several parameters: the wound area, the coverage of the wound relative to the total area, the average wound width, and the standard deviation of the wound width [69]. Micrographs captured at 0, 12, 24, 36 and 48 h of the four wells containing or not 4-AP are illustrated in Figure 20 for HaCaT cells and Figure 21 for HFFF2 cells.

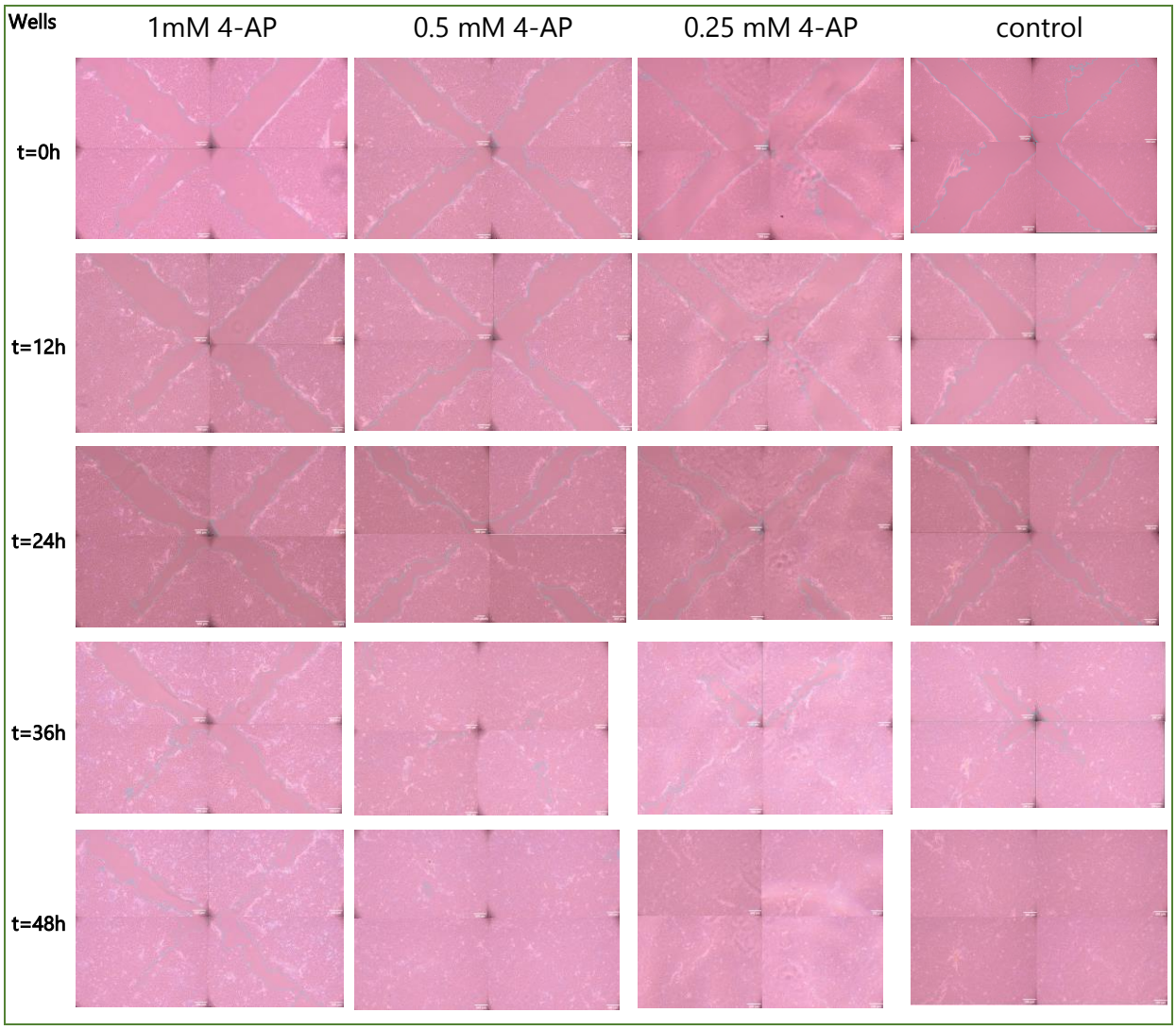

Figure 20- Micrographs captured at 0, 12, 24, 36 and 48h for wells containing 4-AP at a concentration of 1mM, 0.5 mM and 0.25 mM and a control well for HaCaT cells. Scale bar: 200 µm.

The blue lines were identified by the plugin as the boundaries used to define the region of interest, specifically the wound area. The accuracy of automatic gap detection diminishes as the gap approaches closure, where some parts of the gap are missed. As depicted in the Figure 20 and Figure 21, 12 h after the application of 4-AP, the wound remained open in both cell types. However, due to their morphology, fibroblasts appeared more dispersed during migration, resulting in a visibly larger wound area. In contrast, HaCaT cells maintained closer contact

with one another. At 24 h, both wounds showed notable closure compared to the initial state, with HaCaT cells exhibiting a more advanced closure than HFFF2 cells. By 48 h, the wound areas had significantly reduced for both cell types. In HaCaT cells, the wounds with 0.5 mM, 0.25 mM, and control had completely closed. In both cell types, it was observed that the monolayer of cells moved over time in two dimensions, similarly to the process called sheet migration. This type of collective cell migration observed in this wound healing assay has also been identified by other researchers [93] [94] in studies on tissue injury.

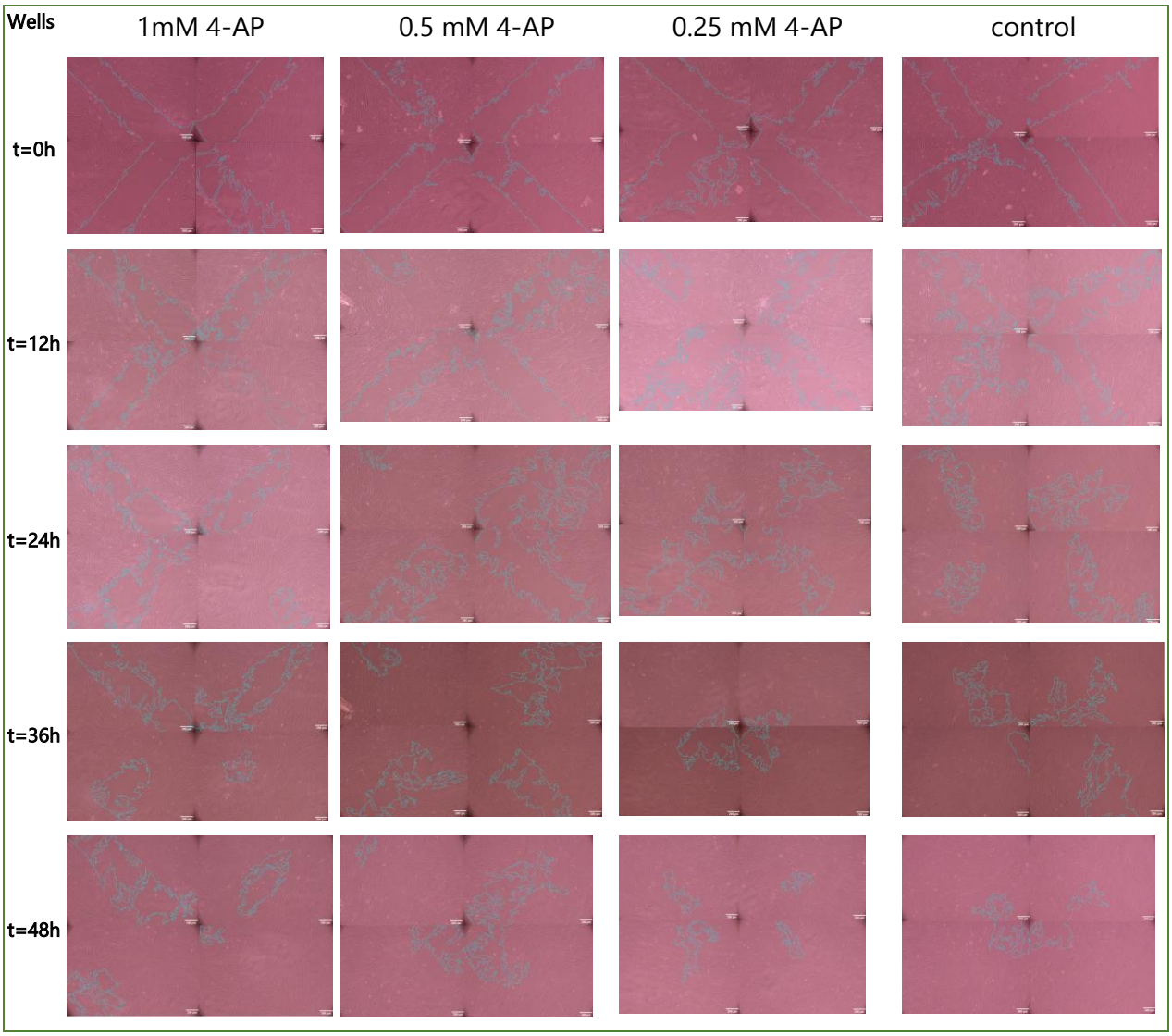

Figure 21- Micrographs captured at 0, 12, 24, 36 and 48h for wells containing 4-AP at 1mM, 0.5 mM and 0.25 mM as well as for control for HFFF2 cells. Scale bar: 200 µm.

When the cell monolayer encounters open space, such as the gap formed in a wound healing assay, a sophisticated coordination of molecular interactions, biochemical signals and mechanical forces, which characterizes sheet migration, is activated [95], [96], [97], [98], [99], [100]. According to some authors, it is a typical behaviour of epithelial and endothelial

monolayers that move in two dimensions, preserving their cell-to-cell connections [101], [102], [103], [104], [105]. Although sheet migration is generally defined by the presence of cell-to-cell connections, Bindschadler *et. al* [106] also observed this behaviour in fibroblasts, suggesting that even in the absence of tight cell-cell connections, fibroblasts may still display sheet migration characteristics. The gap area as a function of time is illustrated in Figure 22A for HaCaT cells and Figure 22B for HFFF2 cells, which shows the progression of wound closure throughout the duration of the assay. It is evident that, in both cases, the wound area decreases over time, as expected. During the initial hours for HFFF2 cells, there is a slight increase in the wound area due to cellular migration, as cells rearrange and the gap momentarily widens, which is detected and quantified by the software as additional space.

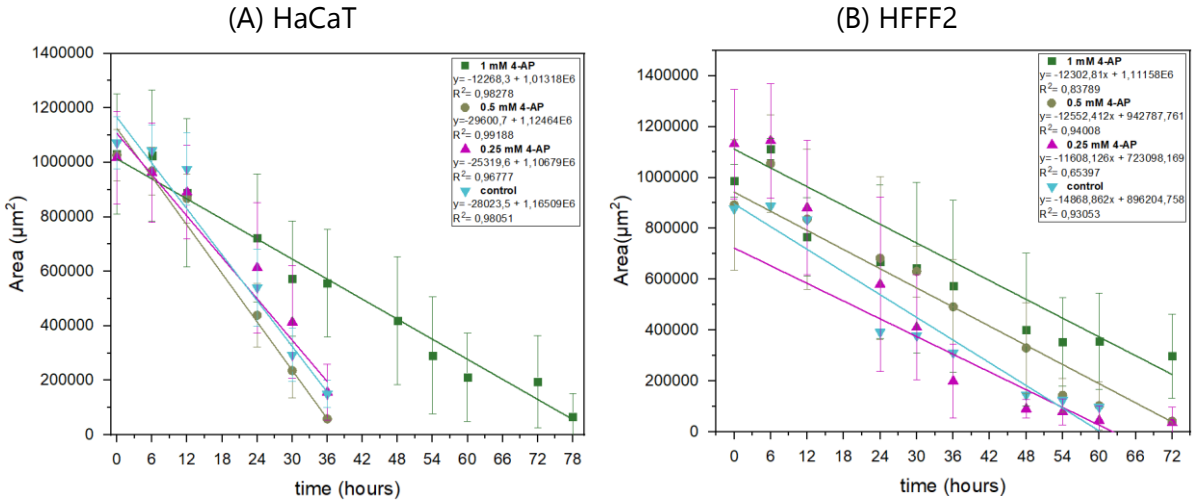

Figure 22- Scratch area (µm^2) as a function of time (h); **(A)** in HaCaT cells; **(B)** in HFFF2 cells. Wells contained 4-AP at a concentration of 1 mM, 0.5 mM, and 0.25 mM. Data is expressed as mean±SD. (n=4).

As shown in Figure 22, conditioned medium containing 4-AP did not enhance wound healing in an *in vitro* epidermal model when compared to the control. The time in which the wound areas approached zero varied in the wells depending on the respective 4-AP concentrations. This difference is more pronounced in the well that contained higher amount of 4-AP, which took more time to close the wound. In HaCaT cells, the wound area nearly reached zero by 36 h in wells with 0.5 mM, 0.25 mM and control, whereas for well with 1 mM, this occurred after 78 h. In HFFF2 cells, wells with 0.25 mM and control control neared complete closure by 48 h, while with 0.5 mM achieved this at 54 h. Comparing both cell types, HFFF2 cells took significantly longer to close the wound, exhibiting consistently larger wound areas over time. Furthermore, the wound area reduction rate in HFFF2 cells was the slowest. The experimental data were fitted to a linear regression using Origin *software*, and the Pearson correlation coefficient was obtained to assess the statistical relationship between the time variable and the

area variable. As expected, the obtained coefficients were negative, indicating an inverse proportionality between these continuous variables. The coefficients were close to -1 (for example, Pearson's r for 1 mM of HaCaT cells is -0,99135), demonstrating a strong and adequate fit of the data. The data fits a linear equation, and the coefficient of determination (R^2) for each cell type and well is presented in Figure 22. As shown in Figure 23, wound closure rates were higher in the presence of lower 4-AP concentrations for HaCaT cells throughout the assay, reaching their maximum at 48 h while 1 mM was at 60 % of wound closure. At higher concentrations 1 mM, wound closure progressed more slowly. For HFFF2 cells, the presence of 4-AP affected wound closure in a similar manner across wells with 1 mM, 0.5 mM and 0.25 mM, regardless of the 4-AP concentration. Notably, HFFF2 cells required more time to achieve substantial wound closure compared to HaCaT cells. In the control groups for both cell lines, wound closure proceeded more efficiently, achieving maximal closure in a shorter time. Although 4-AP did not inhibit wound closure, it slowed the process.

The linear fit was obtained, with the equations of the lines and the coefficient of determination (R^2) for each cell type and each well provided in the respective images in Figure 23. The Pearson correlation coefficient between wound closure and time was found to be positive, as expected.

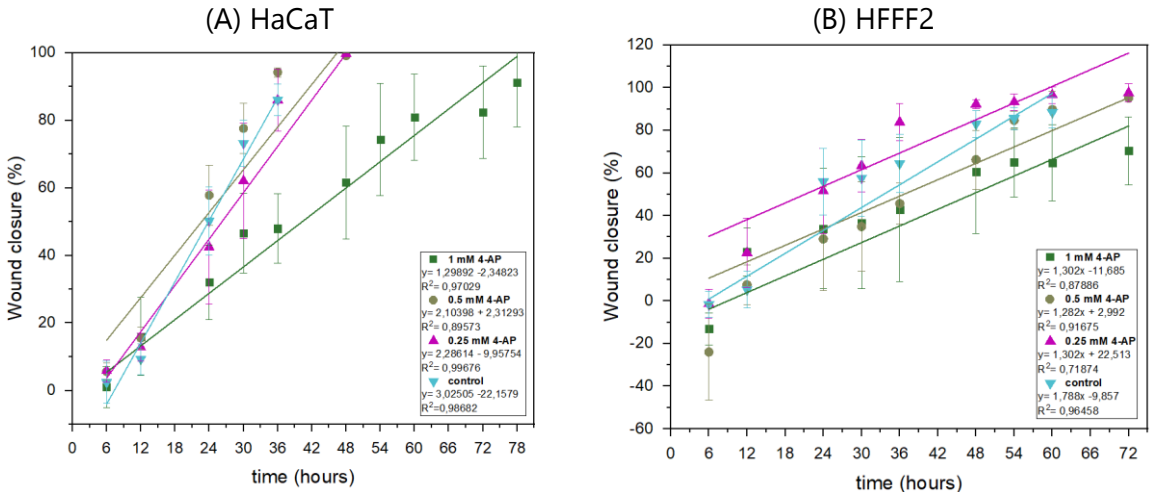

Figure 23- Percentage of closure area. **A.** in HaCaT cells **B.** in HFFF2 cells. Wells contained 4-AP at a concentration of 1 mM, 0.5 mM, and 0.25 mM. Data is expressed as mean±SD. (n=4).

The scratch width was also obtained by the plugin, as shown in Figure 24. For HaCaT cells, the scratch width decreased from 500 µm to nearly zero in control after 42 h and in wells with 0.5 mM and 0.25 mM after 48 h. At 72 h, the scratch width in 1 mM was approximately 100 µm. For HFFF2 cells, the scratch width declined from 500 µm to nearly zero in control after

66 h, and at 72 h 1 mM still had a 300 µm scratch, and 0.5 mM and 0.25 mM had an around100 µm scratch.

Similarly to wound closure, higher concentrations of 4-AP resulted in a slower reduction of scratch width, and HaCaT cells reached minimum values quicker. The standard deviation at each time point is generally higher for the HFFF2 cell line compared to the HaCaT cells, suggesting differences in the migration behavior of the cells.

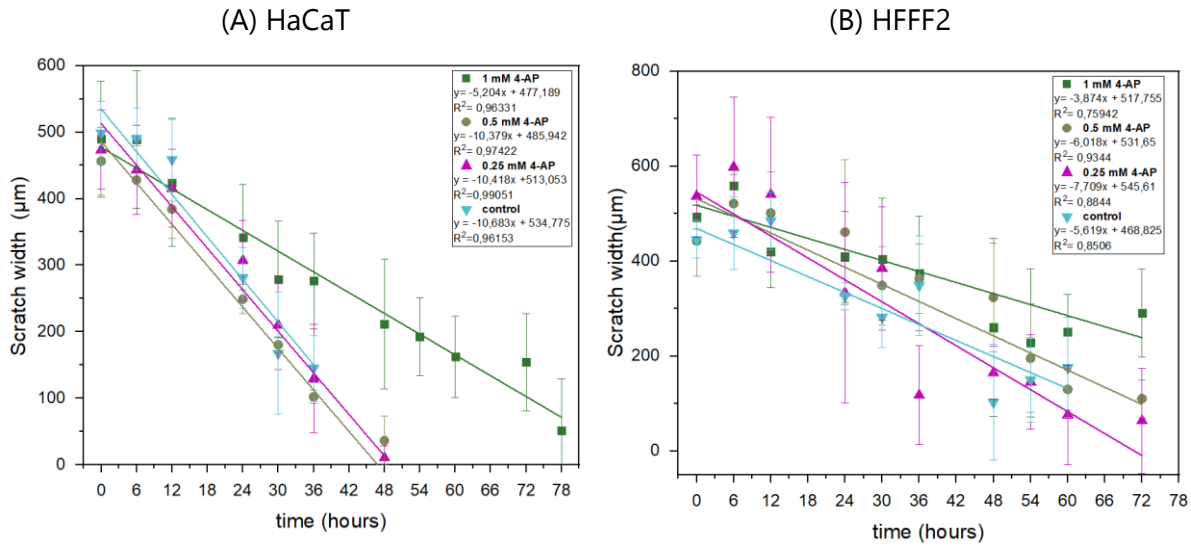

Figure 24- Scratch width. **A.** in HaCaT cells **B.** in HFFF2 cells. Wells contained 4-AP at a concentration of 1 mM, 0.5 mM, and 0.25 mM. Data is expressed as mean±SD. (n=4).

Observing Figure 25, for HaCaT cells, wells with lower 4-AP concentration, exhibited an average migration rate of 7 µm/h, whereas 1 mM displayed a lower rate of 4.5 µm/h. In HFFF2 cells, 0.25 mM demonstrated the highest migration rate, reaching 4.5 µm/h, followed by control at 3 µm/h, 1 mM at 2 µm/h, and 0.5mM with the lowest rate of 0.5 µm/h. Therefore 4-AP concentrations showed no direct effect on the cellular rate migration.

Treatment of fibroblasts and keratinocytes with 4-AP solutions did not hinder cell migration or disrupt wound healing within a 2D cell culture system. Over the course of the experiment, cell migration displayed considerable variability and heterogeneity, likely due to a rapid initial migration phase that gradually slowed.

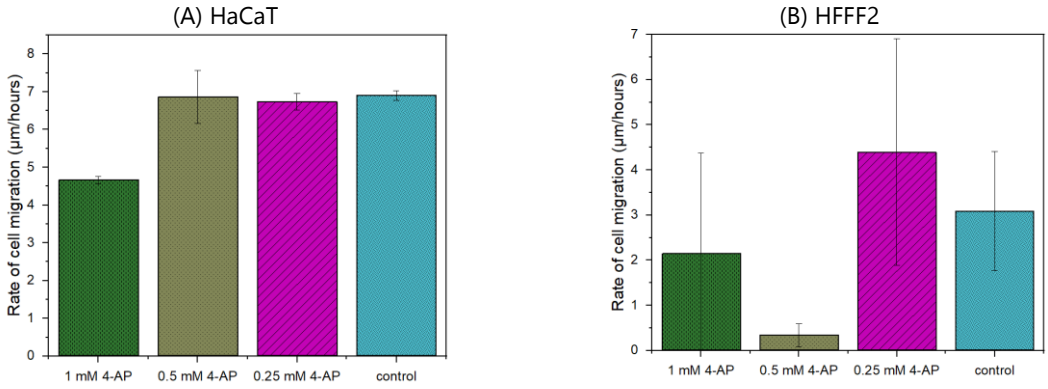

Figure 25- Rate of cell Migration. **A.** in HaCaT cells **B.** in HFFF2 cells. Wells contained 4-AP at a concentration of 1 mM, 0.5 mM, and 0.25 mM. Data is expressed as mean±SD. (n=4).

3.2 Neurite Outgrowth Assays

To investigate whether 4-AP induces differentiation of SH-SY5Y cells and influences neurite outgrowth, elongation, and synapse formation, SH-SY5Y were cultured on the produced membranes. RA was used as a differentiation agent due to its ability to inhibit cell growth and promote differentiation [107], [108], [109].

The fluorescent dye DAPI, used in all membranes, allowed the visualization of cell nucleus. The results obtained through fluorescence microscopy are presented in Apendix A.1. The most relevant results, where a well-defined nucleus was observed, are represented in Figures 26, 27, 28, 29 and 30.

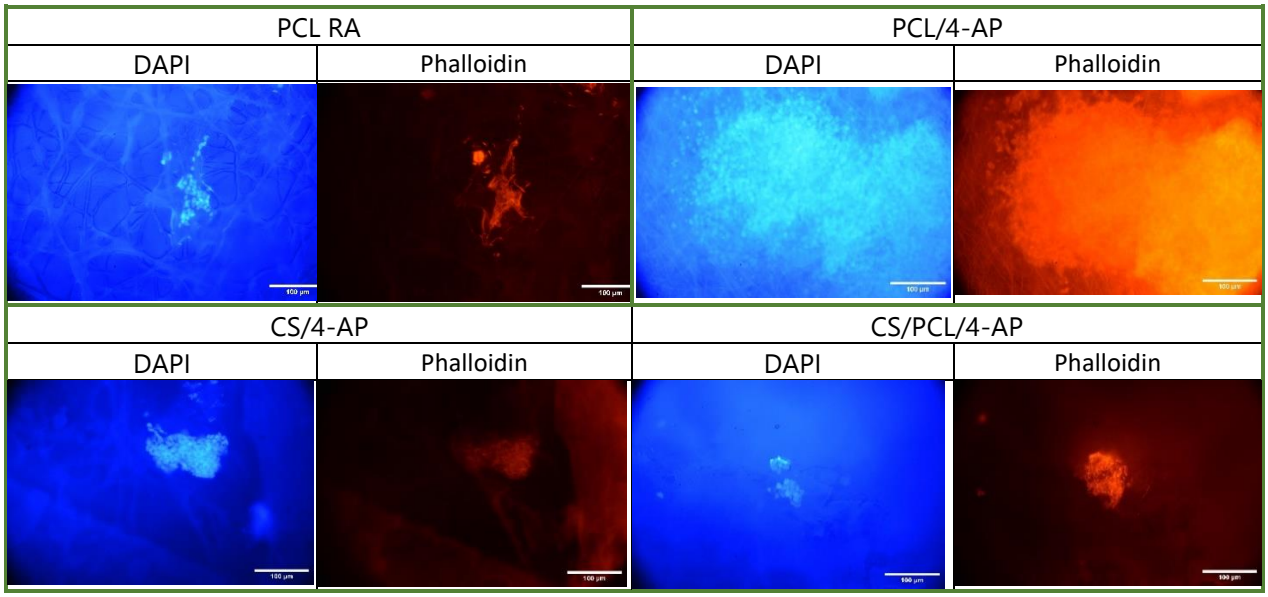

Figure 26- Fluorescence images of SH-SY5Y cells in the membranes. Samples were marked with DAPI and Phalloidin. Scale bar: 100 µm.

Phalloidin was used to visualize filamentous actin (F-actin), a key cytoskeletal protein involved in the formation of neurites and actin filaments [110]. No filaments were observed, which indicate the absence of neurites, Figure 26. Results showed that cells tend to grow in clusters. Undifferentiated cells tend to grow in clusters, these cells do not express mature neuronal markers [111].

In the samples treated with the secondary anti-mouse antibody, MAP-2, a protein expressed during the differentiation of SH-SY5Y cells, expression was detected, with a strong fluorescence signal, mainly in the PCL membranes, Figure 27.

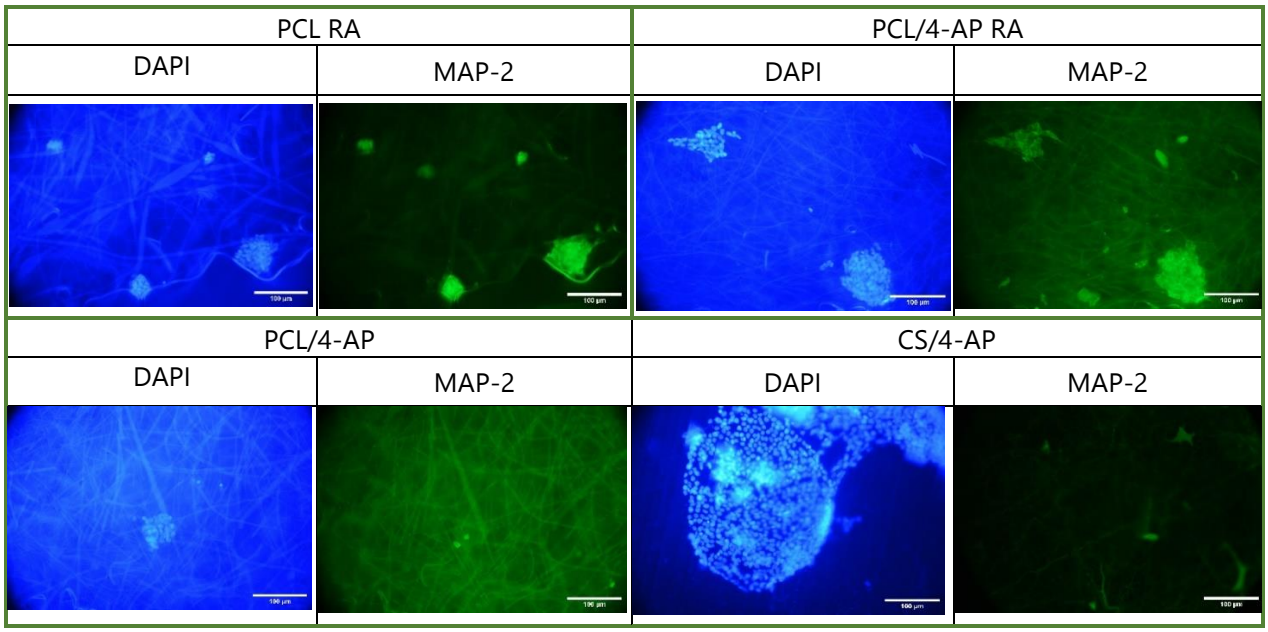

Figure 27- Fluorescence images of SH-SY5Y cells in PCL and CS membranes. Samples were marked with DAPI and MAP-2. Scale bar: 100 µm.

The results suggests that SH-SY5Y cells could be initiating neuronal maturation, to become functionally more similar to neurons, since MAP-2 is a marker for mature neurons [112], [113], [114] by stabilizing and organizing microtubules, which are essential for neurite outgrowth and synapse formation. However, the few cells detected have a rounded appearance, no well-defined dendritic extensions were observed, highlighting that the suggested neuronal maturation may still be at an early stage.

Between the images with nucleus DAPI stained, Figure 27, RA treatment induced neurite development in PCL membranes, indicating SH-SY5Y cell differentiation, while 4-AP alone did not. In PCL/4-AP membranes with RA, differentiation was observed, suggesting 4-AP may enhance RA effect. PCL/4-AP and CS/4-AP both without RA demonstrated a weak MAP-2 fluorescence signal, indicating that SH-SY5Y differentiation did not occur, since these cells normally do not express MAP-2 until they begin to differentiate.

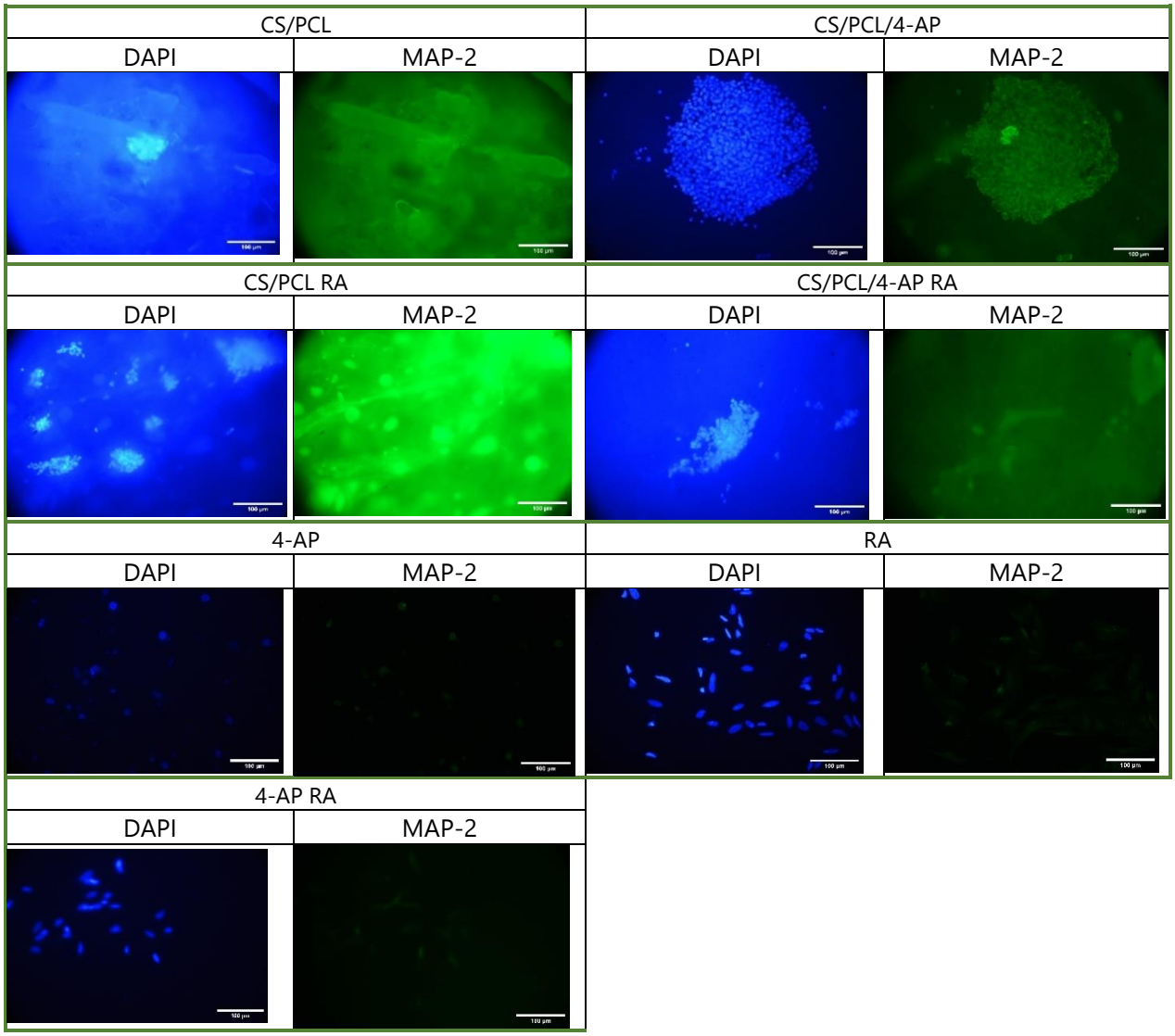

Figure 28- Fluorescence images of SH-SY5Y cells in CS/PCL membranes and control. Samples were marked with DAPI and MAP-2. Scale bar: 100 µm.

According to the control, it was observed that RA, whether in the presence or absence of 4-AP, did not alter the differentiation outcome. Moreover, 4-AP showed no significant influence on cell differentiation. RA demonstrated a markedly superior ability to induce differentiation, as confirmed by fluorescence, highlighting its effectiveness in promoting this process.

In PCL/4-AP membranes treated with RA and stained for MAP-2, Figure 29, captured at the same site but with different focal planes suggest that cells have infiltrated the membrane. This level of infiltration could imply enhanced cellular migration and potentially greater scaffold-cell interactions.

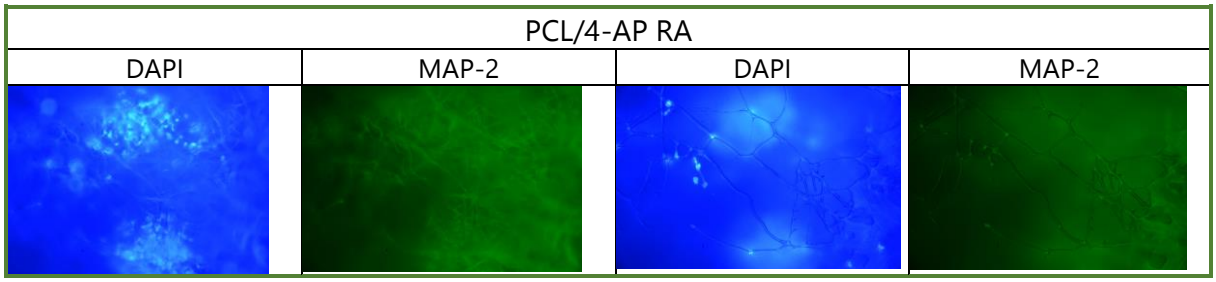

Figure 29- Fluorescence images of SH-SY5Y cells in the membranes. Samples were marked with DAPI and MAP-2. Scale bar: 100 µm.

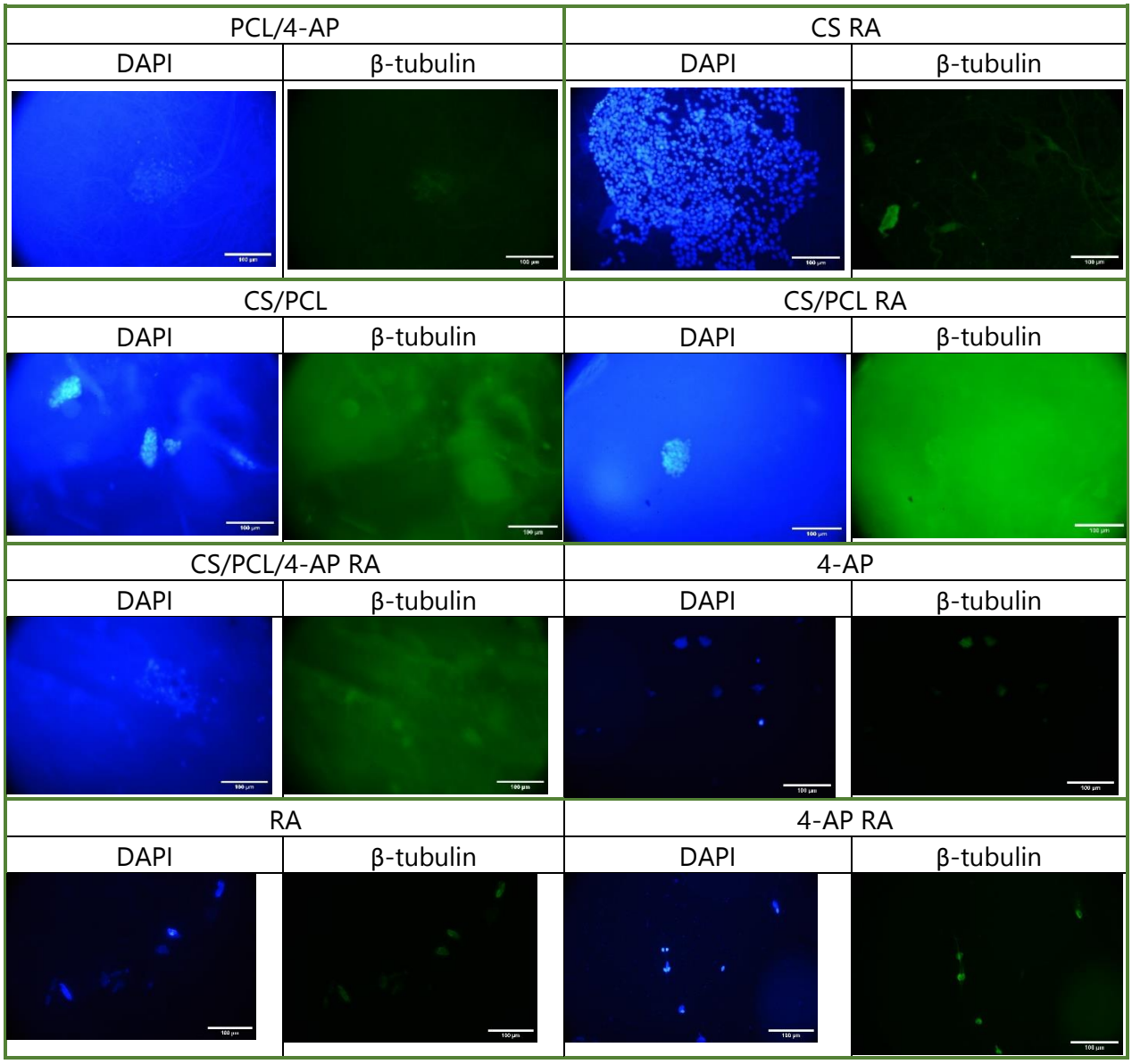

Figure 30- Fluorescence images of SH-SY5Y cells in the membranes. Samples were marked with DAPI and β-Tubulin. Scale bar: 100 µm.

In samples treated with anti-rabbit secondary antibodies, β-tubulin expression was strongly detected in CS/PCL- based membranes, suggesting that SH-SY5Y cells are acquiring

neuronal characteristics. However, there is an absence of clearly defined, elongated neurites extending from the cell body and no visible microtubules indicating full cytoskeletal maturation. β-tubulin III, a key component of the neuronal cytoskeleton, is typically expressed during SH-SY5Y differentiation [109], [112], contributing to the formation of neurites [115] and increased neuronal complexity, signalling the cells advancement toward a mature neuronal state. In the images with DAPI-stained nucleus, (Figure 30) in CS/PCL membranes, it is challenging to discern the results due to the autofluorescence of the membranes and their irregular structure.

RA can facilitate differentiation, as evidenced by fluorescence in the control samples, consistent with the MAP-2 images. In the control, the absence of membranes, 4-AP appears to enhance the effects of RA, with cells displaying a more elongated morphology. In the majority of samples treated with RA, neurite development was observed, indicating successful differentiation of SH-SY5Y cells. In some samples, 4-AP appeared to enhance the expression of neuronal markers. Additional replicates should be performed, and a fluorescence intensity analysis should be conducted to further confirm differentiation.

4

Conclusions and future work

In this work, electrospun nanofiber membranes composed of CS, PCL, and CS/PCL, with and without the incorporation of 4-AP, were produced and characterized. The electrospinning technique successfully generated membranes with high porosity, closely resembling the structure of ECM, which is highly suitable for TE applications.

The study focused on some membrane characteristics that could influence mechanisms of controlled drug delivery. For membranes without 4-AP, the results are generally aligned with findings in the literature. The incorporation of 4-AP into the membranes positively influenced certain properties, such as fiber diameter and membrane swelling behaviour particularly in CS/PCL/4-AP and PCL/4-AP formulations, when compared to CS/PCL and PCL, respectively.

The 4-AP delivery results- 918 µg, CS, 202 µg of PCL and 788 µg CS/PCL, corresponding to the onset of the controlled release phase - are non-toxic to the cells, as indicated by the cell cytotoxicity data.

The wound healing assay, conducted with fibroblasts and keratinocytes, revealed that after 48 hours, the wound areas had significantly reduced for both cell types. In keratinocytes cells, the wounds treated with 0.5 mM and 0.25 mM of 4-AP were completely closed.

The behaviour of the membranes, particularly those of CS/PCL, appeared promising, but for the possibility of developing a 4-AP delivery system using these biodegradable and biocompatible membranes, suitable for applications in skin regeneration and reinnervation requires more investigation. Further studies are required to comprehensively understand the release kinetics and behaviour of the membranes in controlled drug release. Future work should include additional replicates to ensure reproducibility and statistical significance. Moreover, implementing complementary assays, such as MTS or WST, DNA quantification using the PicoGreen assay could help identify potential cytotoxic effects associated with the interaction between PCL and 4-AP. These efforts will deepen the understanding of the membranes therapeutic potential and optimize their design for regenerative medicine applications.

BIBLIOGRAPHY

[1] "J. M., L. 'NOVAthesis Word Templatefor FCT-NOVA'. (2021).".

[2] A. L. Rippa *et al.*, "Regeneration of Dermis: Scarring and Cells Involved.," *Cells*, vol. 8, no. 6, Jun. 2019, doi: 10.3390/cells8060607.

[3] K. Vig *et al.*, "Advances in Skin Regeneration Using Tissue Engineering.," *Int J Mol Sci*, vol. 18, no. 4, Apr. 2017, doi: 10.3390/ijms18040789.

[4] N. Lebonvallet *et al.*, "New insights into the roles of myofibroblasts and innervation during skin healing and innovative therapies to improve scar innervation.," *Exp Dermatol*, vol. 27, no. 9, pp. 950–958, Sep. 2018, doi: 10.1111/exd.13681.

[5] J. R. Yu *et al.*, "Current and Future Perspectives on Skin Tissue Engineering: Key Features of Biomedical Research, Translational Assessment, and Clinical Application.," *Adv Healthc Mater*, vol. 8, no. 5, p. e1801471, Mar. 2019, doi: 10.1002/adhm.201801471.

[6] T. Weng *et al.*, "Regeneration of skin appendages and nerves: current status and further challenges," *J Transl Med*, vol. 18, no. 1, p. 53, Dec. 2020, doi: 10.1186/s12967-020-02248-5.

[7] J. Peng *et al.*, "Nerve–stem cell crosstalk in skin regeneration and diseases," *Trends Mol Med*, vol. 28, no. 7, pp. 583–595, Jul. 2022, doi: 10.1016/j.molmed.2022.04.005.

[8] T. Kornfeld *et al.*, "Reconstruction of Critical Nerve Defects Using Allogenic Nerve Tissue: A Review of Current Approaches," *Int J Mol Sci*, vol. 22, no. 7, p. 3515, Mar. 2021, doi: 10.3390/ijms22073515.

[9] R. Supra *et al.*, "Therapeutic Potential of 'Smart' Exosomes in Peripheral Nerve Regeneration," *Journal of Biotechnology and Biomedicine*, vol. 06, no. 02, 2023, doi: 10.26502/jbb.2642-91280082.

[10] M. Bernard *et al.*, "Peripheral Nerve Matrix Hydrogel Promotes Recovery after Nerve Transection and Repair.," *Plast Reconstr Surg*, vol. 152, no. 3, pp. 458e–467e, Sep. 2023, doi: 10.1097/PRS.0000000000010261.

[11] J. Gu *et al.*, "Surgical repair of a 30 mm long human median nerve defect in the distal forearm by implantation of a chitosan-PGA nerve guidance conduit," *J Tissue Eng Regen Med*, vol. 6, no. 2, pp. 163–168, Feb. 2012, doi: 10.1002/term.407.

[12] Z. Rao *et al.*, "Biomaterial-Based Schwann Cell Transplantation and Schwann Cell-Derived Biomaterials for Nerve Regeneration.," *Front Cell Neurosci*, vol. 16, p. 926222, 2022, doi: 10.3389/fncel.2022.926222.

[13] R. Supra *et al.*, "Peripheral Nerve Regeneration: Opportunities and Challenges," *Journal of Spine Research and Surgery*, vol. 05, no. 01, 2023, doi: 10.26502/fjsrs0052.

[14] K. Dzobo *et al.*, "Advances in Regenerative Medicine and Tissue Engineering: Innovation and Transformation of Medicine.," *Stem Cells Int*, vol. 2018, p. 2495848, 2018, doi: 10.1155/2018/2495848.

[15] G. C. Gurtner *et al.*, "Wound repair and regeneration.," *Nature*, vol. 453, no. 7193, pp. 314–21, May 2008, doi: 10.1038/nature07039.

[16] A. Balakrishnan *et al.*, "Insights Into the Role and Potential of Schwann Cells for Peripheral Nerve Repair From Studies of Development and Injury.," *Front Mol Neurosci*, vol. 13, p. 608442, 2020, doi: 10.3389/fnmol.2020.608442.

[17] Y. Sowa *et al.*, "Direct Conversion of Human Fibroblasts into Schwann Cells that Facilitate Regeneration of Injured Peripheral Nerve In Vivo.," *Stem Cells Transl Med*, vol. 6, no. 4, pp. 1207–1216, Apr. 2017, doi: 10.1002/sctm.16-0122.

[18] J.-W. Jang *et al.*, "Review: Scaffold Characteristics, Fabrication Methods, and Biomaterials for the Bone Tissue Engineering," *International Journal of Precision Engineering and Manufacturing*, vol. 24, no. 3, pp. 511–529, Mar. 2023, doi: 10.1007/s12541-022-00755-7.

[19] H. Baniasadi *et al.*, "Fabrication and characterization of conductive chitosan/gelatin-based scaffolds for nerve tissue engineering.," *Int J Biol Macromol*, vol. 74, pp. 360–6, Mar. 2015, doi: 10.1016/j.ijbiomac.2014.12.014.

[20] C. A. M. Ferreira *et al.*, "Multifunctional Gelatin/Chitosan Electrospun Wound Dressing Dopped with Undaria pinnatifida Phlorotannin-Enriched Extract for Skin Regeneration.," *Pharmaceutics*, vol. 13, no. 12, Dec. 2021, doi: 10.3390/pharmaceutics13122152.

[21] K. Tseng *et al.*, "4-Aminopyridine promotes functional recovery and remyelination in acute peripheral nerve injury," *EMBO Mol Med*, vol. 8, no. 12, pp. 1409–1420, Dec. 2016, doi: 10.15252/emmm.201506035.

[22] C. Smith *et al.*, "In Vitro electrophysiological activity of nerispirdine, a novel 4-aminopyridine derivative.," *Clin Exp Pharmacol Physiol*, vol. 36, no. 11, pp. 1104–9, Nov. 2009, doi: 10.1111/j.1440-1681.2009.05200.x.

[23] M. K. Haidar *et al.*, "Atorvastatin-loaded nanosprayed chitosan nanoparticles for peripheral nerve injury," *Bioinspired, Biomimetic and Nanobiomaterials*, vol. 9, no. 2, pp. 74–84, Jun. 2020, doi: 10.1680/jbibn.19.00006.

[24] Z. Edis *et al.*, "Nanocarriers-Mediated Drug Delivery Systems for Anticancer Agents: An Overview and Perspectives," *Int J Nanomedicine*, vol. Volume 16, pp. 1313–1330, Feb. 2021, doi: 10.2147/IJN.S289443.

[25] L. Mazzeo *et al.*, "Drug Delivery With Membranes Systems," in *Current Trends and Future Developments on (Bio-) Membranes*, Elsevier, 2019, pp. 291–309. doi: 10.1016/B978-0-12-813606-5.00010-5.

[26] Y. Enjavi *et al.*, "Drug delivery systems," in *Current Trends and Future Developments on (Bio-) Membranes*, Elsevier, 2024, pp. 209–228. doi: 10.1016/B978-0-323-90258-8.00018-3.

[27] R. Sao *et al.*, "Multifunctional Drug Delivery Systems Using Inorganic Nanomaterials: A Review," *J Nanosci Nanotechnol*, vol. 15, no. 3, pp. 1960–1972, Mar. 2015, doi: 10.1166/jnn.2015.9761.

[28] W. B. Liechty *et al.*, "Polymers for Drug Delivery Systems," *Annu Rev Chem Biomol Eng*, vol. 1, no. 1, pp. 149–173, Jun. 2010, doi: 10.1146/annurev-chembioeng-073009-100847.

[29] V. M. K. R. V. V. R. S.RAMAKRISHNA, "DESIGN AND EVALUATION OF DRUG RELEASE KINETICS OF MELOXICAM SUSTAINED RELEASE MATRIX TABLETS," *Int J Curr Pharm Res*, vol. 4, no. 1, pp. 90–99, 2012.

[30] H. Baishya, "Application of Mathematical Models in Drug Release Kinetics of Carbidopa and Levodopa ER Tablets," *J Dev Drugs*, vol. 06, no. 02, 2017, doi: 10.4172/2329-6631.1000171.

[31] P. Trucillo, "Drug Carriers: A Review on the Most Used Mathematical Models for Drug Release," *Processes*, vol. 10, no. 6, p. 1094, May 2022, doi: 10.3390/pr10061094.

[32] S. Klein *et al.*, "Peripheral Nerve Regeneration-Adipose-Tissue-Derived Stem Cells Differentiated by a Three-Step Protocol Promote Neurite Elongation via NGF Secretion.," *Cells*, vol. 11, no. 18, Sep. 2022, doi: 10.3390/cells11182887.

[33] S. R. Gomes *et al.*, "In vitro evaluation of crosslinked electrospun fish gelatin scaffolds," *Materials Science and Engineering: C*, vol. 33, no. 3, pp. 1219–1227, Apr. 2013, doi: 10.1016/j.msec.2012.12.014.

[34] L. Alonso *et al.*, "Stem cells of the skin epithelium," *Proceedings of the National Academy of Sciences*, vol. 100, no. suppl_1, pp. 11830–11835, Sep. 2003, doi: 10.1073/pnas.1734203100.

[35] M. Blais *et al.*, "Improvement of Nerve Regeneration in Tissue-Engineered Skin Enriched with Schwann Cells," *Journal of Investigative Dermatology*, vol. 129, no. 12, pp. 2895–2900, Dec. 2009, doi: 10.1038/jid.2009.159.

[36] R. A. F. Clark *et al.*, "Tissue engineering for cutaneous wounds.," *J Invest Dermatol*, vol. 127, no. 5, pp. 1018–29, May 2007, doi: 10.1038/sj.jid.5700715.

[37] G. R. Evans *et al.*, "In vivo evaluation of poly(L-lactic acid) porous conduits for peripheral nerve regeneration.," *Biomaterials*, vol. 20, no. 12, pp. 1109–15, Jun. 1999, doi: 10.1016/s0142-9612(99)00010-1.

[38] S. N. Deshmukh *et al.*, "Enigmatic insight into collagen.," *J Oral Maxillofac Pathol*, vol. 20, no. 2, pp. 276–83, 2016, doi: 10.4103/0973-029X.185932.

[39] T. D. Allen *et al.*, "The contraction of collagen matrices by dermal fibroblasts," *J Ultrastruct Res*, vol. 83, no. 2, pp. 205–219, May 1983, doi: 10.1016/S0022-5320(83)90078-3.

[40] S. O. Sarrigiannidis *et al.*, "A tough act to follow: collagen hydrogel modifications to improve mechanical and growth factor loading capabilities," *Mater Today Bio*, vol. 10, p. 100098, Mar. 2021, doi: 10.1016/j.mtbio.2021.100098.

[41] J. Dulnik *et al.*, "Crosslinking of Gelatin in Bicomponent Electrospun Fibers.," *Materials (Basel)*, vol. 14, no. 12, Jun. 2021, doi: 10.3390/ma14123391.

[42] H. S. Koh *et al.*, "Enhancement of neurite outgrowth using nano-structured scaffolds coupled with laminin.," *Biomaterials*, vol. 29, no. 26, pp. 3574–82, Sep. 2008, doi: 10.1016/j.biomaterials.2008.05.014.

[43] T. B. Ngo *et al.*, "Poly(L-Lactide) microfilaments enhance peripheral nerve regeneration across extended nerve lesions," *J Neurosci Res*, vol. 72, no. 2, pp. 227–238, Apr. 2003, doi: 10.1002/jnr.10570.

[44] C. Loyo *et al.*, "Effect of Gelatin Coating and GO Incorporation on the Properties and Degradability of Electrospun PCL Scaffolds for Bone Tissue Regeneration," *Polymers (Basel)*, vol. 16, no. 1, p. 129, Dec. 2023, doi: 10.3390/polym16010129.

[45] E. Kijeńska *et al.*, "Electrospun bio-composite P(LLA-CL)/collagen I/collagen III scaffolds for nerve tissue engineering.," *J Biomed Mater Res B Appl Biomater*, vol. 100, no. 4, pp. 1093–102, May 2012, doi: 10.1002/jbm.b.32676.

[46] F. Seidi *et al.*, "Chitosan-based blends for biomedical applications," *Int J Biol Macromol*, vol. 183, pp. 1818–1850, Jul. 2021, doi: 10.1016/j.ijbiomac.2021.05.003.

[47] M. Zuber *et al.*, "Chitin and Chitosan Based Blends, Composites and Nanocomposites," 2013, pp. 55–119. doi: 10.1007/978-3-642-20940-6_3.

[48] N. Naseri *et al.*, "Electrospun chitosan-based nanocomposite mats reinforced with chitin nanocrystals for wound dressing," *Carbohydr Polym*, vol. 109, pp. 7–15, Aug. 2014, doi: 10.1016/j.carbpol.2014.03.031.

[49] E. M Ahmed *et al.*, "Chitosan-based nanocomposites: preparation and characterization for food packing industry," *Mater Res Express*, vol. 8, no. 2, p. 025017, Feb. 2021, doi: 10.1088/2053-1591/abe791.

[50] S. Ahmed *et al.*, "Chitosan Based Scaffolds and Their Applications in Wound Healing," *Achievements in the Life Sciences*, vol. 10, no. 1, pp. 27–37, Jun. 2016, doi: 10.1016/j.als.2016.04.001.

[51] F. J. Xu *et al.*, "Surface functionalization of polycaprolactone films via surface-initiated atom transfer radical polymerization for covalently coupling cell-adhesive biomolecules," *Biomaterials*, vol. 31, no. 12, pp. 3139–3147, Apr. 2010, doi: 10.1016/j.biomaterials.2010.01.032.

[52] H. Bahrami *et al.*, "Human unrestricted somatic stem cells loaded in nanofibrous PCL scaffold and their healing effect on skin defects," *Artif Cells Nanomed Biotechnol*, vol. 44, no. 6, pp. 1556–1560, Aug. 2016, doi: 10.3109/21691401.2015.1062390.

[53] M. T. KHAN a *et al.*, "Effect of Different Solvent Systems on Fiber Morphology and Property of Electrospun PCL Nano Fibers," *Tekstil ve Muhendis*, vol. 28, no. 122, pp. 61–76, Jun. 2021, doi: 10.7216/1300759920212812201.

[54] M. Bartnikowski *et al.*, "Degradation mechanisms of polycaprolactone in the context of chemistry, geometry and environment," *Prog Polym Sci*, vol. 96, pp. 1–20, Sep. 2019, doi: 10.1016/j.progpolymsci.2019.05.004.

[55] T. Valente *et al.*, "Polymer blending or fiber blending: A comparative study using chitosan and poly(ε-caprolactone) electrospun fibers," *J Appl Polym Sci*, vol. 136, no. 11, Mar. 2019, doi: 10.1002/app.47191.

[56] N. I. M. Fadilah *et al.*, "Functionalised-biomatrix for wound healing and cutaneous regeneration: future impactful medical products in clinical translation and precision medicine.," *Front Bioeng Biotechnol*, vol. 11, p. 1160577, 2023, doi: 10.3389/fbioe.2023.1160577.

[57] P. Pal *et al.*, "Bilayered nanofibrous 3D hierarchy as skin rudiment by emulsion electrospinning for burn wound management," *Biomater Sci*, vol. 5, no. 9, pp. 1786–1799, 2017, doi: 10.1039/C7BM00174F.

[58] M. Fallah-Darrehchi *et al.*, "Conductive conduit based on electrospun poly (l-lactide-co-D, l-lactide) nanofibers containing 4-aminopyridine-loaded molecularly imprinted poly (methacrylic acid) nanoparticles used for peripheral nerve regeneration," *Int J Biol Macromol*, vol. 190, pp. 499–507, Nov. 2021, doi: 10.1016/j.ijbiomac.2021.09.009.

[59] S. Rodríguez-Rangel *et al.*, "Structure-activity relationship studies of four novel 4-aminopyridine K+ channel blockers," *Sci Rep*, vol. 10, no. 1, p. 52, Jan. 2020, doi: 10.1038/s41598-019-56245-w.

[60] A. Caggiano *et al.*, "Effects of dalfampridine and its metabolites on cloned human potassium channels K_v 1.1, K_v 1.2, and K_v 1.4 expressed in human embryonic kidney cells," *J Drug Assess*, vol. 2, no. 1, pp. 58–66, Apr. 2013, doi: 10.3109/21556660.2013.791623.

[61] I. Kostadinova *et al.*, "4-aminopyridine – the new old drug for the treatment of neurodegenerative diseases," *Pharmacia*, vol. 66, no. 2, pp. 67–74, Jul. 2019, doi: 10.3897/pharmacia.66.e35976.

[62] M. G. Jagadeeshaprasad *et al.*, "4-Aminopyridine Induces Nerve Growth Factor to Improve Skin Wound Healing and Tissue Regeneration.," *Biomedicines*, vol. 10, no. 7, Jul. 2022, doi: 10.3390/biomedicines10071649.

[63] I. Martínez-González *et al.*, "Effect of varying the restriction degree of 4-aminopyridine release from HPMC matrices on the mechanism controlling the process.," *Int J Pharm*, vol. 257, no. 1–2, pp. 253–64, May 2003, doi: 10.1016/s0378-5173(03)00150-9.

[64] D. Querido *et al.*, "Study on the Incorporation of Chitosan Flakes in Electrospun Polycaprolactone Scaffolds," *Polymers (Basel)*, vol. 14, no. 8, p. 1496, Apr. 2022, doi: 10.3390/polym14081496.

[65] N. Zhu *et al.*, "Biofabrication of Tissue Scaffolds," in *Advances in Biomaterials Science and Biomedical Applications*, InTech, 2013. doi: 10.5772/54125.

[66] S. Gomes *et al.*, "Evaluation of nanofibrous scaffolds obtained from blends of chitosan, gelatin and polycaprolactone for skin tissue engineering," *Int J Biol Macromol*, vol. 102, pp. 1174–1185, Sep. 2017, doi: 10.1016/j.ijbiomac.2017.05.004.

[67] T. Vieira *et al.*, "Electrospun Polycaprolactone Membranes Expanded with Chitosan Granules for Cell Infiltration," *Polymers (Basel)*, vol. 16, no. 4, p. 527, Feb. 2024, doi: 10.3390/polym16040527.

[68] F. Farshi Azhar *et al.*, "Fabrication and characterization of chitosan–gelatin/nanohydroxyapatite–polyaniline composite with potential application in tissue engineering scaffolds," *Des Monomers Polym*, vol. 17, no. 7, pp. 654–667, Oct. 2014, doi: 10.1080/15685551.2014.907621.

[69] A. Suarez-Arnedo *et al.*, "An image J plugin for the high throughput image analysis of in vitro scratch wound healing assays," *PLoS One*, vol. 15, no. 7, p. e0232565, Jul. 2020, doi: 10.1371/journal.pone.0232565.

[70] S. R. Gomes *et al.*, "In vitro and in vivo evaluation of electrospun nanofibers of PCL, chitosan and gelatin: A comparative study," *Materials Science and Engineering: C*, vol. 46, pp. 348–358, Jan. 2015, doi: 10.1016/j.msec.2014.10.051.

[71] R. Lungu *et al.*, "Double functionalization of chitosan based nanofibers towards biomaterials for wound healing," *React Funct Polym*, vol. 167, p. 105028, Oct. 2021, doi: 10.1016/j.reactfunctpolym.2021.105028.

[72] H.-H. Kao *et al.*, "Polycaprolactone/Chitosan Composite Nanofiber Membrane as a Preferred Scaffold for the Culture of Mesothelial Cells and the Repair of Damaged Mesothelium," *Int J Mol Sci*, vol. 23, no. 17, p. 9517, Aug. 2022, doi: 10.3390/ijms23179517.

[73] M. M. Lim *et al.*, "In Vitro Biological Evaluation of Electrospun Polycaprolactone/Gelatine Nanofibrous Scaffold for Tissue Engineering," *J Nanomater*, vol. 2015, no. 1, Jan. 2015, doi: 10.1155/2015/303426.

[74] D. Poddar *et al.*, "Chitosan-coated pore wall polycaprolactone three-dimensional porous scaffolds fabricated by porogen leaching method for bone tissue engineering: a comparative study on blending technique to fabricate scaffolds," *Prog Biomater*, vol. 10, no. 4, pp. 281–297, Dec. 2021, doi: 10.1007/s40204-021-00172-5.

[75] N. V. Gupta *et al.*, "Investigation of Swelling Behavior and Mechanical Properties of a pH-Sensitive Superporous Hydrogel Composite.," *Iran J Pharm Res*, vol. 11, no. 2, pp. 481–93, 2012.

[76] K. Phillipson *et al.*, "Thermal analysis FTIR spectroscopy of poly(ε-caprolactone)," *Thermochim Acta*, vol. 595, pp. 74–82, Nov. 2014, doi: 10.1016/j.tca.2014.08.027.

[77] K. Pieklarz *et al.*, "STRUCTURAL AND BIOLOGICAL CHARACTERISTICS OF SELF-ORGANISING CHITOSAN HYDROGELS," *Prog Chem Appl Chitin Deriv*, vol. 26, pp. 191–199, Sep. 2021, doi: 10.15259/PCACD.26.017.

[78] M. Sowjanya *et al.*, "Polymers used in the Designing of Controlled Drug Delivery System," *Res J Pharm Technol*, vol. 10, no. 3, p. 903, 2017, doi: 10.5958/0974-360X.2017.00168.8.

[79] M. Prabaharan *et al.*, "Chitosan-Based Particles as Controlled Drug Delivery Systems," *Drug Deliv*, vol. 12, no. 1, pp. 41–57, Jan. 2004, doi: 10.1080/10717540590889781.

[80] C. S. Brazel *et al.*, "Modeling of drug release from Swellable polymers," *European Journal of Pharmaceutics and Biopharmaceutics*, vol. 49, no. 1, pp. 47–58, Jan. 2000, doi: 10.1016/S0939-6411(99)00058-2.

[81] T. Higuchi, "Mechanism of sustained-action medication. Theoretical analysis of rate of release of solid drugs dispersed in solid matrices," *J Pharm Sci*, vol. 52, no. 12, pp. 1145–1149, Dec. 1963, doi: 10.1002/jps.2600521210.

[82] H. Lapidus *et al.*, "Some Factors Affecting the Release of a Water-Soluble Drug from a Compressed Hydrophilic Matrix," *J Pharm Sci*, vol. 55, no. 8, pp. 840–843, Aug. 1966, doi: 10.1002/jps.2600550818.

[83] R. W. Korsmeyer *et al.*, "Mechanisms of solute release from porous hydrophilic polymers," *Int J Pharm*, vol. 15, no. 1, pp. 25–35, May 1983, doi: 10.1016/0378-5173(83)90064-9.

[84] M.-L. Laracuente *et al.*, "Zero-order drug delivery: State of the art and future prospects," *Journal of Controlled Release*, vol. 327, pp. 834–856, Nov. 2020, doi: 10.1016/j.jconrel.2020.09.020.

[85] N. S. Awad *et al.*, "Ultrasound-Responsive Nanocarriers in Cancer Treatment: A Review.," *ACS Pharmacol Transl Sci*, vol. 4, no. 2, pp. 589–612, Apr. 2021, doi: 10.1021/acsptsci.0c00212.

[86] G. Patel *et al.*, "Ganciclovir Loaded Chitosan Nanoparticles: Preparation and Characterization," *J Nanomed Nanotechnol*, vol. 07, no. 06, 2016, doi: 10.4172/2157-7439.1000411.

[87] M. D. A. Muhsin *et al.*, "Effects of Chemical Conjugation of L-Leucine to Chitosan on Dispersibility and Controlled Release of Drug from a Nanoparticulate Dry Powder Inhaler Formulation," *Mol Pharm*, vol. 13, no. 5, pp. 1455–1466, May 2016, doi: 10.1021/acs.molpharmaceut.5b00859.

[88] H. Thai *et al.*, "Characterization of chitosan/alginate/lovastatin nanoparticles and investigation of their toxic effects in vitro and in vivo," *Sci Rep*, vol. 10, no. 1, p. 909, Jan. 2020, doi: 10.1038/s41598-020-57666-8.

[89] J. Pérez Quiñones *et al.*, "Novel drug delivery systems: Chitosan conjugates covalently attached to steroids with potential anticancer and agrochemical activity," *Carbohydr Polym*, vol. 84, no. 3, pp. 858–864, Mar. 2011, doi: 10.1016/j.carbpol.2010.12.007.

[90] J. H. Lee *et al.*, "Controlled drug release from pharmaceutical nanocarriers," *Chem Eng Sci*, vol. 125, pp. 75–84, Mar. 2015, doi: 10.1016/j.ces.2014.08.046.

[91] T. Vieira *et al.*, "Electrospun biodegradable chitosan based-poly(urethane urea) scaffolds for soft tissue engineering," *Materials Science and Engineering: C*, vol. 103, p. 109819, Oct. 2019, doi: 10.1016/j.msec.2019.109819.

[92] Z. B. Kaya *et al.*, "Optimizing SH-SY5Y cell culture: exploring the beneficial effects of an alternative media supplement on cell proliferation and viability," *Sci Rep*, vol. 14, no. 1, p. 4775, Feb. 2024, doi: 10.1038/s41598-024-55516-5.

[93] P. Martin *et al.*, "Parallels between tissue repair and embryo morphogenesis," *Development*, vol. 131, no. 13, pp. 3021–3034, Jul. 2004, doi: 10.1242/dev.01253.

[94] C. A. Reinhart-King, "Chapter 3 Endothelial Cell Adhesion and Migration," 2008, pp. 45–64. doi: 10.1016/S0076-6879(08)02003-X.

[95] J. H. Kim *et al.*, "Propulsion and navigation within the advancing monolayer sheet," *Nat Mater*, vol. 12, no. 9, pp. 856–863, Sep. 2013, doi: 10.1038/nmat3689.

[96] P. Vitorino *et al.*, "Modular control of endothelial sheet migration," *Genes Dev*, vol. 22, no. 23, pp. 3268–3281, Dec. 2008, doi: 10.1101/gad.1725808.

[97] D. A. Chapnick *et al.*, "Leader cell positioning drives wound-directed collective migration in TGFβ-stimulated epithelial sheets," *Mol Biol Cell*, vol. 25, no. 10, pp. 1586–1593, May 2014, doi: 10.1091/mbc.e14-01-0697.

[98] F.-C. Tsai *et al.*, "A polarized Ca2+, diacylglycerol and STIM1 signalling system regulates directed cell migration," *Nat Cell Biol*, vol. 16, no. 2, pp. 133–144, Feb. 2014, doi: 10.1038/ncb2906.

[99] X. Trepat *et al.*, "Plithotaxis and emergent dynamics in collective cellular migration," *Trends Cell Biol*, vol. 21, no. 11, pp. 638–646, Nov. 2011, doi: 10.1016/j.tcb.2011.06.006.

[100] M. Reffay *et al.*, "Interplay of RhoA and mechanical forces in collective cell migration driven by leader cells," *Nat Cell Biol*, vol. 16, no. 3, pp. 217–223, Mar. 2014, doi: 10.1038/ncb2917.

[101] O. Ilina *et al.*, "Mechanisms of collective cell migration at a glance," *J Cell Sci*, vol. 122, no. 18, pp. 3203–3208, Sep. 2009, doi: 10.1242/jcs.036525.

[102] P. Friedl *et al.*, "Collective cell migration in morphogenesis, regeneration and cancer," *Nat Rev Mol Cell Biol*, vol. 10, no. 7, pp. 445–457, Jul. 2009, doi: 10.1038/nrm2720.

[103] P. Friedl *et al.*, "Plasticity of cell migration: a multiscale tuning model," *Journal of Cell Biology*, vol. 188, no. 1, pp. 11–19, Jan. 2010, doi: 10.1083/jcb.200909003.

[104] S. R. K. Vedula *et al.*, "Collective Cell Migration: A Mechanistic Perspective," *Physiology*, vol. 28, no. 6, pp. 370–379, Nov. 2013, doi: 10.1152/physiol.00033.2013.

[105] P. Rørth, "Collective Cell Migration," *Annu Rev Cell Dev Biol*, vol. 25, no. 1, pp. 407–429, Nov. 2009, doi: 10.1146/annurev.cellbio.042308.113231.

[106] M. Bindschadler *et al.*, "Sheet migration by wounded monolayers as an emergent property of single-cell dynamics," *J Cell Sci*, vol. 120, no. 5, pp. 876–884, Mar. 2007, doi: 10.1242/jcs.03395.

[107] A. P. Kalinovskii *et al.*, "Retinoic Acid-Differentiated Neuroblastoma SH-SY5Y Is an Accessible In Vitro Model to Study Native Human Acid-Sensing Ion Channels 1a (ASIC1a)," *Biology (Basel)*, vol. 11, no. 2, p. 167, Jan. 2022, doi: 10.3390/biology11020167.

[108] M. M. Shipley *et al.*, "Differentiation of the SH-SY5Y Human Neuroblastoma Cell Line," *Journal of Visualized Experiments*, no. 108, Feb. 2016, doi: 10.3791/53193.

[109] R. Bilginer Kartal *et al.*, "Exploring Neuronal Differentiation Profiles in SH-SY5Y Cells through Magnetic Levitation Analysis," *ACS Omega*, vol. 9, no. 13, pp. 14955–14962, Apr. 2024, doi: 10.1021/acsomega.3c08962.

[110] M. Romani *et al.*, "Phalloidin Staining of Actin Filaments for Visualization of Muscle Fibers in Caenorhabditis elegans," *Bio Protoc*, vol. 11, no. 19, 2021, doi: 10.21769/BioProtoc.4183.

[111] A. Dravid *et al.*, "Optimised techniques for high-throughput screening of differentiated SH-SY5Y cells and application for neurite outgrowth assays," *Sci Rep*, vol. 11, no. 1, p. 23935, Dec. 2021, doi: 10.1038/s41598-021-03442-1.

[112] B. S. Serdar *et al.*, "Comparison of Medium Supplements in Terms of the Effects on the Differentiation of SH-SY5Y Human Neuroblastoma Cell Line," *Neurological*

Sciences and Neurophysiology, vol. 37, no. 2, pp. 82–88, 2020, doi: 10.4103/NSN.NSN_15_20.

[113] D. C. M. Kulatunga *et al.*, "A novel APP splice variant-dependent marker system to precisely demarcate maturity in SH-SY5Y cell-derived neurons," *Sci Rep*, vol. 14, no. 1, p. 12113, May 2024, doi: 10.1038/s41598-024-63005-y.

[114] E. J. H. F. Voogd *et al.*, "Degree of differentiation impacts neurobiological signature and resistance to hypoxia of SH-SY5Y cells," *J Neural Eng*, vol. 20, no. 6, p. 066038, Dec. 2023, doi: 10.1088/1741-2552/ad17f3.

[115] I. L. Targett *et al.*, "Differentiation of SH-SY5Y neuroblastoma cells using retinoic acid and BDNF: a model for neuronal and synaptic differentiation in neurodegeneration," *In Vitro Cell Dev Biol Anim*, Jul. 2024, doi: 10.1007/s11626-024-00948-6.

A

APPENDIX

A.1 Results of differentiation assays

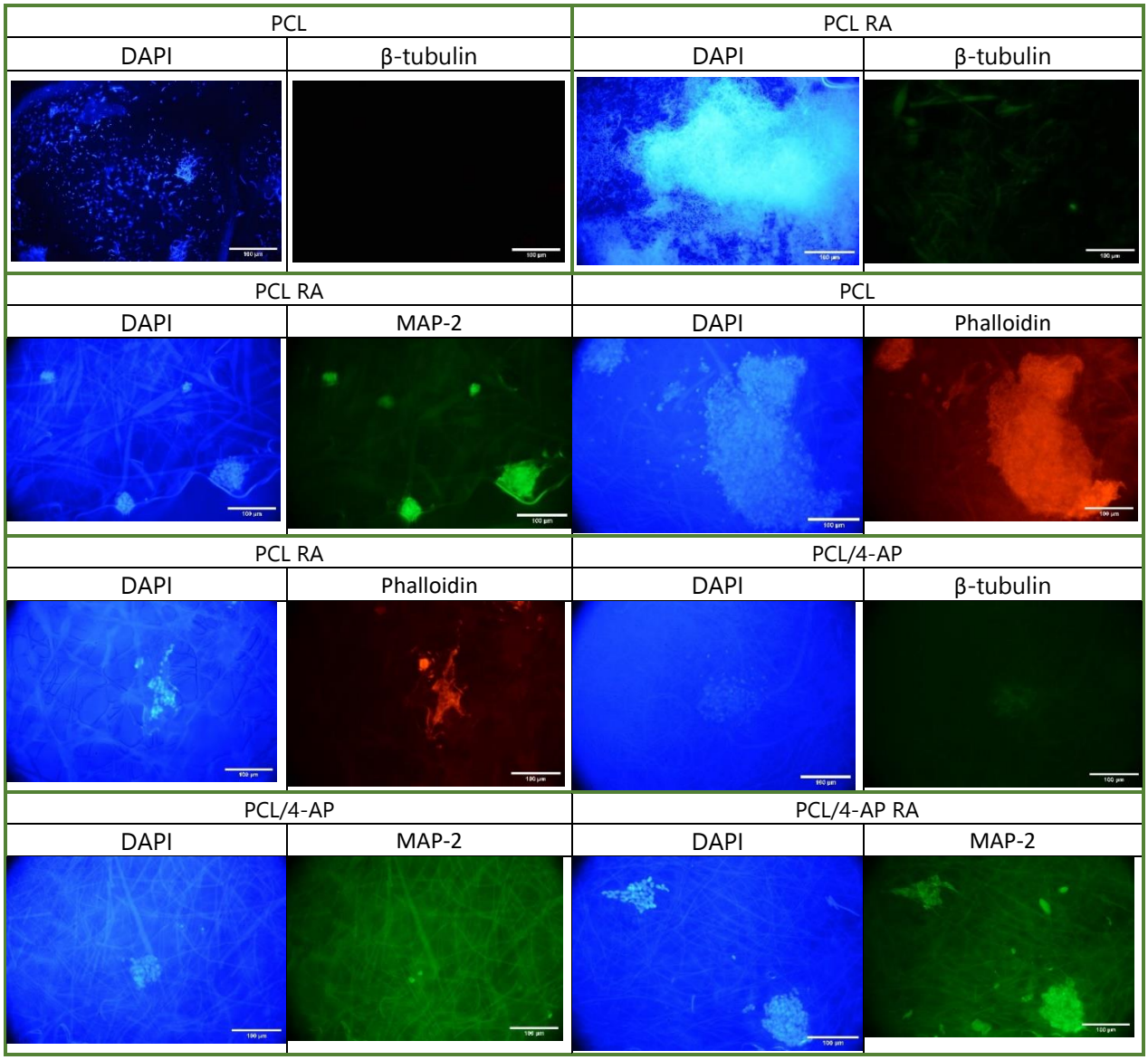

PCL/4-AP		CS	
DAPI	Phalloidin	DAPI	β-tubulin
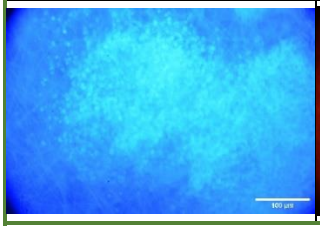	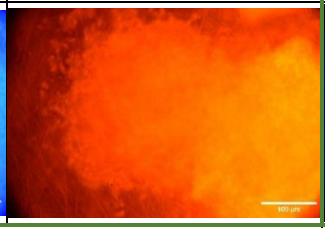	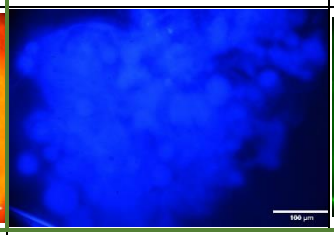	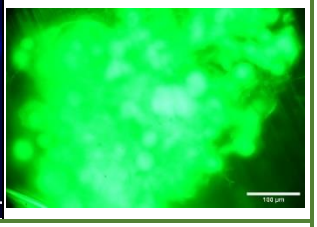
CS		CS RA	
DAPI	MAP-2	DAPI	β-tubulin
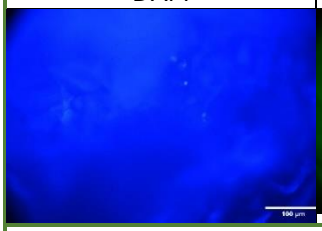	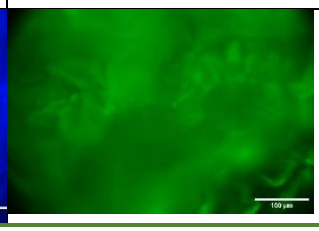	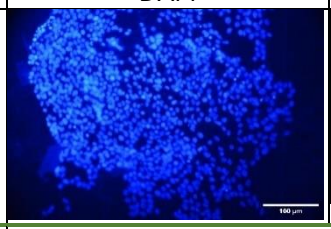	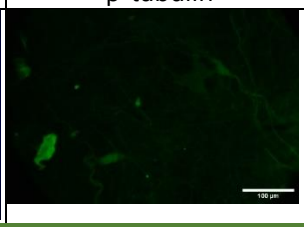
CS RA		CS	
DAPI	MAP-2	DAPI	Phalloidin
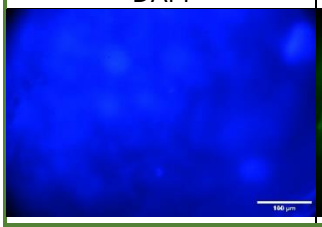	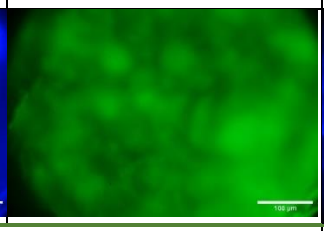	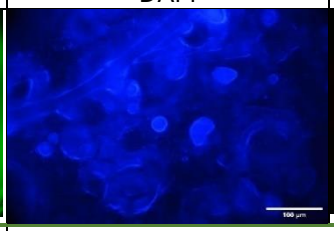	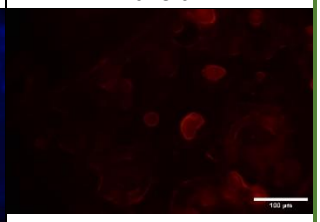
CS/4-AP		CS RA	
DAPI	β-tubulin	DAPI	Phalloidin
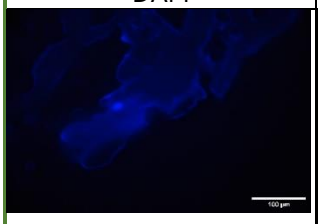	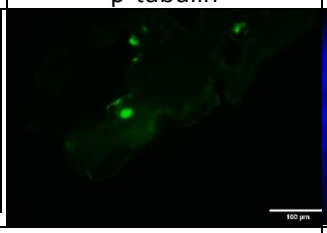	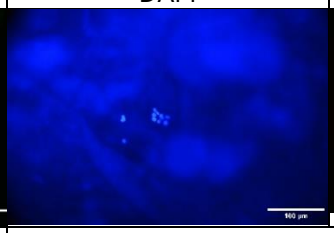	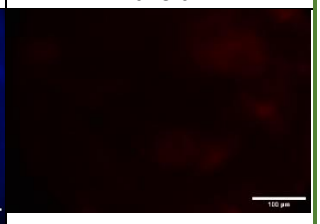
CS/4-AP RA		CS/4-AP	
DAPI	β-tubulin	DAPI	MAP-2
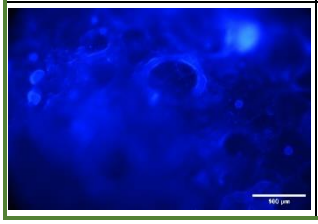	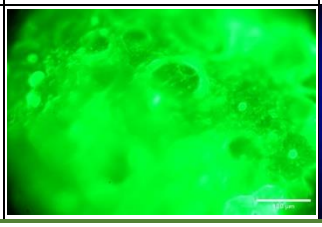	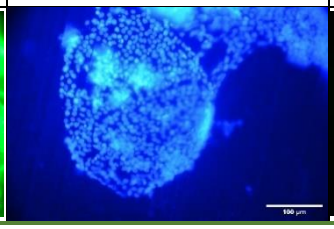	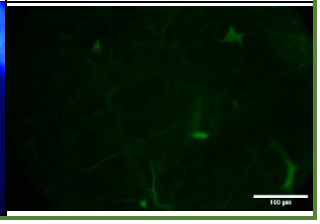

CS/4-AP		CS/4-AP RA	
DAPI	Phalloidin	DAPI	MAP-2
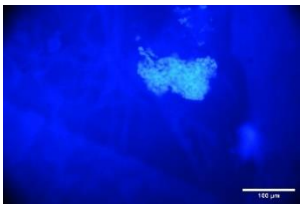	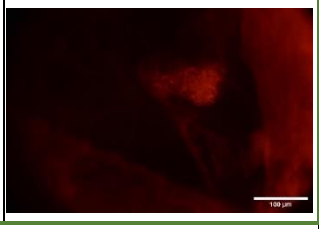	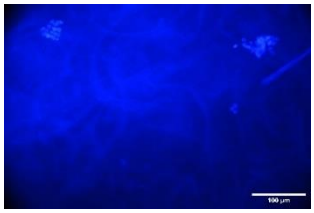	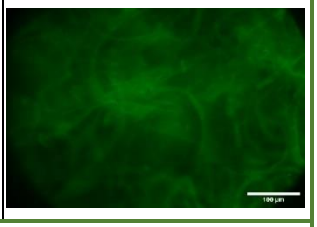
CS/4-AP RA		**CS/PCL**	
DAPI	Phalloidin	DAPI	β-tubulin
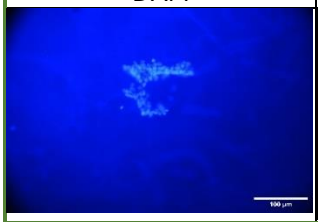	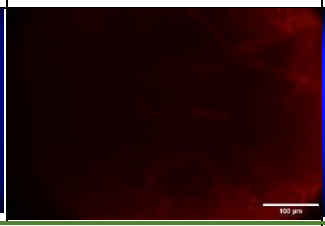	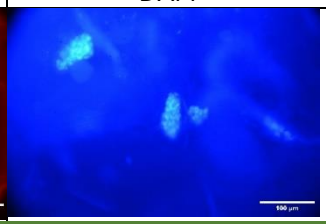	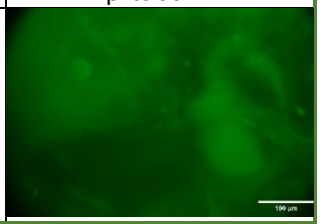
CS/PCL		**CS/PCL RA**	
DAPI	MAP-2	DAPI	β-tubulin
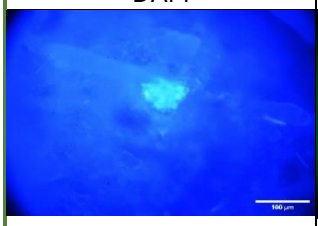	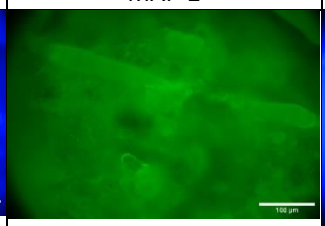	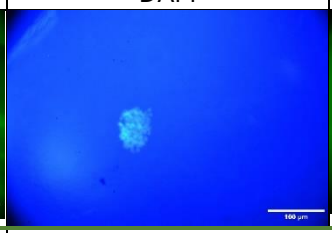	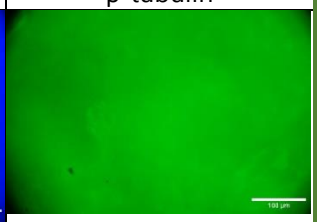
CS/PCL RA		**CS/PCL**	
DAPI	MAP-2	DAPI	Phalloidin
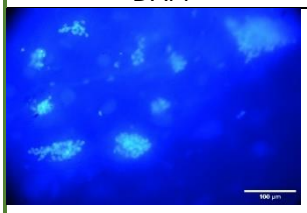	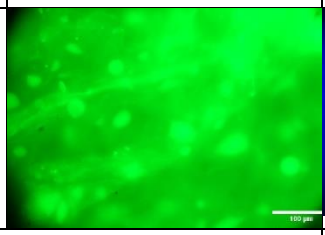	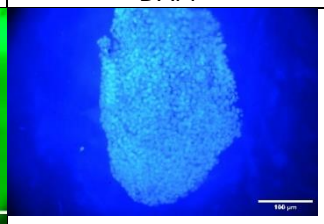	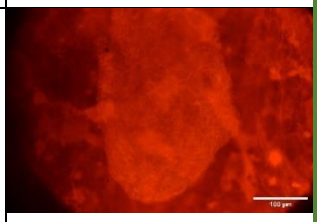
CS/PCL/4-AP		**CS/PCL/4-AP RA**	
DAPI	β-tubulin	DAPI	β-tubulin
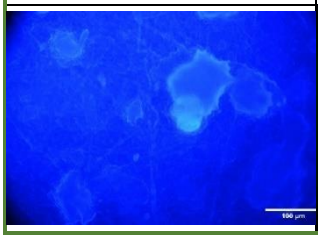	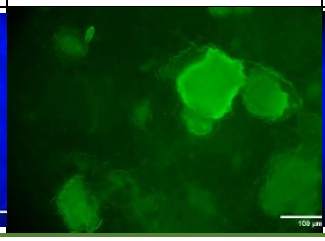	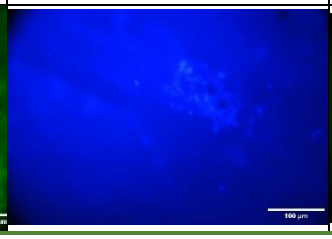	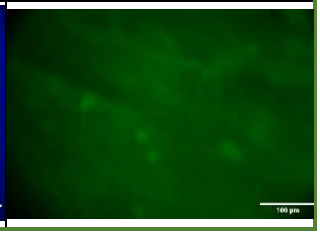

CS/PCL/4-AP		CS/PCL/4-AP	
DAPI	MAP-2	DAPI	Phalloidin
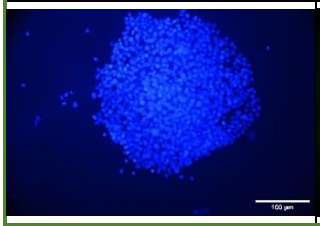	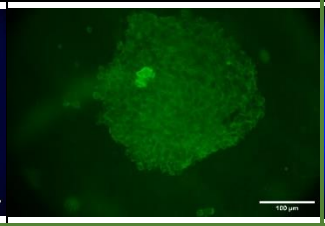	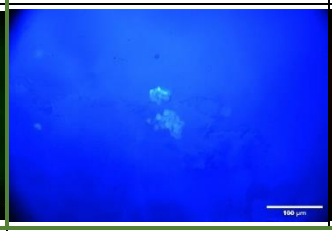	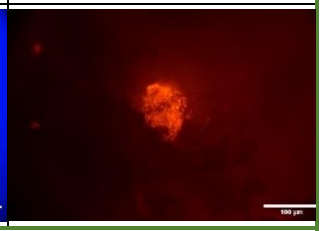
CS/PCL/4-AP RA		4-AP	
DAPI	MAP-2	DAPI	β-tubulin
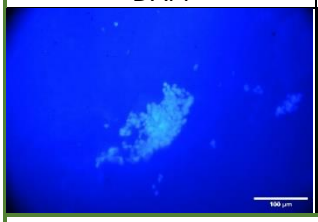	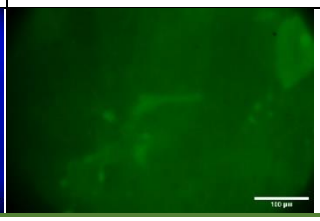	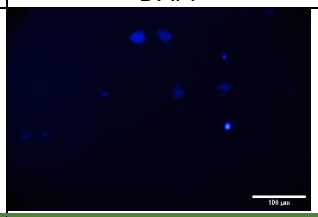	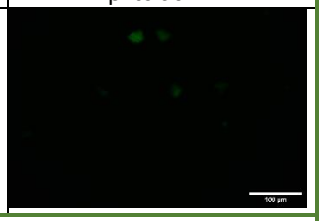
4-AP		No 4-AP and No RA	
DAPI	MAP-2	DAPI	β-tubulin
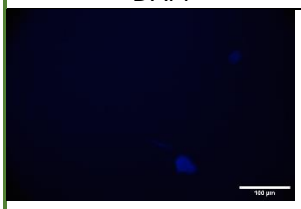	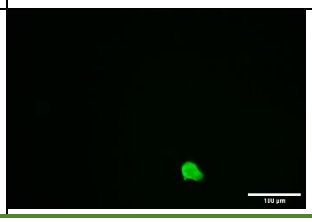	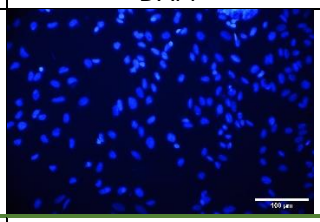	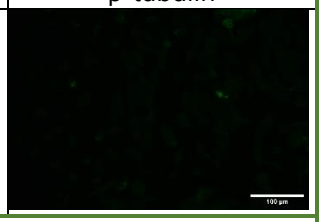
4-AP RA		No 4-AP and No RA	
DAPI	β-tubulin	DAPI	MAP-2
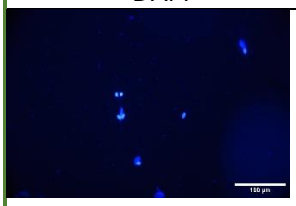	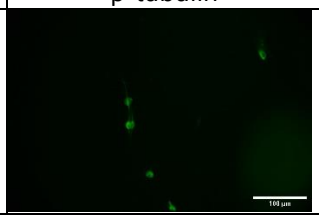	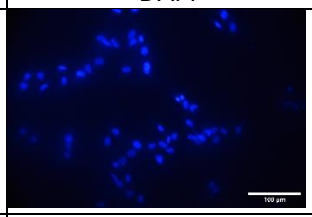	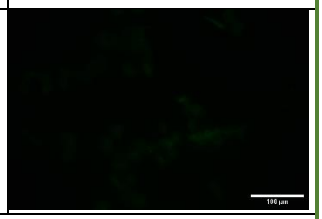
4-AP RA		RA	
DAPI	MAP-2	DAPI	β-tubulin
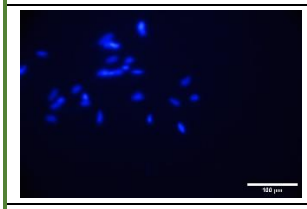	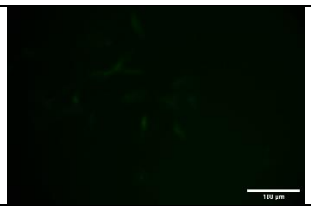	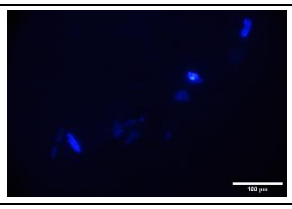	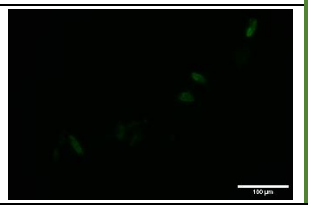
RA			
DAPI	MAP-2